Research Paper

GEOSPHERE

GEOSPHERE, v. 16, no. 5

https://doi.org/10.1130/GES02251.1

13 figures; 1 set of supplemental files

CORRESPONDENCE: blatc005@umn.edu

CITATION: Blatchford, H.J., Klepeis, K.A., Schwartz, J.J., Jongens, R., Turnbull, R.E., Miranda, E.A., Coble, M.A., and Kylander-Clark, A.R.C., 2020, Interplay of Cretaceous transpressional deformation and continental arc magmatism in a long-lived crustal boundary, central Fiordland, New Zealand: Geosphere, v. 16, no. 5, p. 1225–1248, https://doi.org/10.1130/GES02251.1.

Science Editor: Andrea Hampel
Associate Editor: Valero Acocella

Received 3 March 2020
Revision received 31 May 2020
Accepted 24 July 2020

Published online 31 August 2020

Interplay of Cretaceous transpressional deformation and continental arc magmatism in a long-lived crustal boundary, central Fiordland, New Zealand

Hannah J. Blatchford[1,*], Keith A. Klepeis[1], Joshua J. Schwartz[2], Richard Jongens[3], Rose E. Turnbull[4], Elena A. Miranda[2], Matthew A. Coble[5], Andrew R. C. Kylander-Clark[6]

[1]Department of Geology, University of Vermont, Burlington, Vermont 05405, USA
[2]Department of Geological Sciences, California State University Northridge, Northridge, California 91330, USA
[3]Anatoki Geoscience Ltd., Dunedin 9012, New Zealand
[4]GNS Science, Dunedin Research Centre, Dunedin 9054, New Zealand
[5]Department of Geological Sciences, Stanford University, Stanford, California 94305, USA
[6]Department of Earth Science, University of California–Santa Barbara, Santa Barbara, California 93106, USA

ABSTRACT

Recovering the time-evolving relationship between arc magmatism and deformation, and the influence of anisotropies (inherited foliations, crustal-scale features, and thermal gradients), is critical for interpreting the location, timing, and geometry of transpressional structures in continental arcs. We investigated these themes of magma-deformation interactions and preexisting anisotropies within a middle- and lower-crustal section of Cretaceous arc crust coinciding with a Paleozoic boundary in central Fiordland, New Zealand. We present new structural mapping and results of Zr-in-titanite thermometry and U-Pb zircon and titanite geochronology from an Early Cretaceous batholith and its host rock. The data reveal how the expression of transpression in the middle and lower crust of a continental magmatic arc evolved during emplacement and crystallization of the ~2300 km² lower-crustal Western Fiordland Orthogneiss (WFO) batholith. Two structures within Fiordland's architecture of transpressional shear zones are identified. The gently dipping Misty shear zone records syn-magmatic oblique-sinistral thrust motion between ca. 123 and ca. 118 Ma, along the lower-crustal WFO Misty Pluton margin. The subhorizontal South Adams Burn thrust records mid-crustal arc-normal shortening between ca. 114 and ca. 111 Ma. Both structures are localized within and reactivate a recently described >10 km-wide Paleozoic crustal boundary, and show that deformation migrated upwards between ca. 118 and ca. 114 Ma. WFO emplacement and crystallization (mainly 118–115 Ma) coincided with elevated (>750 °C) middle- and lower-crustal Zr-in-titanite temperatures and the onset of mid-crustal cooling at 5.9 ± 2.0 °C Ma^{-1} between ca. 118 and ca. 95 Ma. We suggest that reduced strength contrasts across lower-crustal pluton margins during crystallization caused deformation to migrate upwards into thermally weakened rocks of the mid-crust. The migration was accompanied by partitioning of deformation into domains of arc-normal shortening in Paleozoic metasedimentary rocks and domains that combined shortening and strike-slip deformation in crustal-scale subvertical, transpressional shear zones previously documented in Fiordland. U-Pb titanite dates indicate Carboniferous–Cretaceous (re)crystallization, consistent with reactivation of the inherited boundary. Our results show that spatio-temporal patterns of transpression are influenced by magma emplacement and crystallization and by the thermal structure of a reactivated boundary.

Hannah J. Blatchford http://orcid.org/0000-0001-5741-8086
*Now at Department of Earth & Environmental Sciences, University of Minnesota, Minneapolis, Minnesota 55455, USA

INTRODUCTION

A single magmatic arc system can display impressive heterogeneity with respect to the tempo of magmatism, intrusion geometry, and the presence of inherited structures including old faults, regional foliations, and crustal-scale boundaries. Structures, including ductile shear zones, typically form during arc magmatism (e.g., Tommasi et al., 1994; Mulcahy et al., 2011; Vaughan et al., 2012; Molina-Garza et al., 2015; Miranda and Klepeis, 2016; Klepeis et al., 2016), but we still have limited knowledge of how magmatism and preexisting structures interact with deformation in the crustal column. Importantly, these interactions can change over time and with position in the arc. Because deformation is generally regarded as important for the transfer of heat and mass through the crust (e.g., Whitney et al., 2004; Klepeis et al., 2016; Lehmann et al., 2017), thorough documentation of how deformation and magmatism interact at different depths within arcs through time is necessary for understanding how continental crust is created and modified—processes occurring primarily in magmatic arcs since the Proterozoic (Condie and Kröner, 2013; Condie, 2014; Hawkesworth et al., 2019).

Transpressional deformation, originally defined by Sanderson and Marchini (1984) as the simultaneous application of pure and simple shear acting within a volume to produce horizontal shortening and vertical extrusion, is commonly

spatially and temporally associated with magmatism in Cordilleran arcs (e.g., Tikoff and Saint Blanquat, 1997; Saint Blanquat et al., 1998; Rosenberg, 2004; Zibra et al., 2014). However, apart from observations of strike-slip partitioning of transpressional deformation associated with thermal weakening and rheological contrasts at the margins of middle- to upper-crustal plutons (e.g., Fitch, 1972; Tikoff and Teyssier, 1994; Tikoff and Saint Blanquat, 1997; Saint Blanquat et al., 1998; Philippon and Corti, 2016), there has been little work undertaken to evaluate the impact of spatial and temporal heterogeneities on the expression of transpression in magmatic arcs. Sources of heterogeneity in these settings include magma emplacement tempos, intrusion geometry, and the presence and architecture of inherited structures. Geochronological studies indicate that magmatism in continental arcs commonly display non–steady-state patterns and may include short-lived (5–20 m.y.; Ducea et al., 2015a) flare-up events wherein ≥85% of an arc's magmatic volume is emplaced in only a few million years (e.g., Ducea, 2001; Ducea and Barton, 2007; Chapman et al., 2012; Economos et al., 2012; Otamendi et al., 2012; DeCelles et al., 2015). In addition, pluton geometry and deformation styles typically vary with depth in the arc crustal column. The lower crust appears to be dominated by subhorizontal, tabular intrusions (e.g., Klepeis et al., 2003; Miller et al., 2009; Klepeis et al., 2016; Chan et al., 2017), while plutonic rocks at middle- and upper-crustal levels may be steep-sided (Paterson et al., 2011; Ducea et al., 2015b; Buriticá et al., 2019). Despite recognition of these heterogeneities, we still know relatively little about the extent to which pluton geometry influences the expression of transpression, as well as the response of deformation partitioning to pluton crystallization.

The reactivation of inherited structures (e.g., Holdsworth et al., 1997) can introduce additional complexity to the architecture of continental arcs. Continental arcs tend to be long-lived features that are subject to changes in plate motions and growth by the accretion of outboard arcs and terranes—characteristics that create crustal anisotropies and influence the rates and locations of magma addition. Field-based and modeling studies investigating structural reactivation show that the process can range in scale from small individual fault surfaces to crustal-scale structures formed by terrane accretion, deformation, and magmatism (e.g., Bitencourt and Nardi, 2000; Scott et al., 2011; Miller and Becker, 2014; Klepeis et al., 2019a, 2019b; Nabavi et al., 2020). Inherited structures have both the ability to localize deformation and to act as conduits for the transport of melt and fluids (e.g., Naganjaneyulu and Santosh, 2011; Lu et al., 2012; Klepeis et al., 2019a). This latter process is of particular interest because transport of melt and fluids through the crust has the potential to influence geothermal gradients at mid- and lower-crustal levels (Depine et al., 2008; Schwartz et al., 2016). Therefore, the study of inherited boundaries is important because they record the geological expression of multiple deformation events and deformation-magmatism interactions.

To investigate these topics, we use mid- and lower-crustal exposures of Cretaceous magmatic arc crust in central Fiordland, South Island, New Zealand (Fig. 1). Fiordland hosts a large expanse of mid- and lower-crustal intrusive rock, including the ~2300 km² Western Fiordland Orthogneiss (WFO, Fig. 2), emplaced as part of an Early Cretaceous flare-up event (Allibone et al., 2009b; Schwartz et al., 2017). The region also has a well-preserved record of transpressional deformation active at the same time (e.g., Daczko et al., 2001; Klepeis et al., 2004; Marcotte et al., 2005; Scott et al., 2011; Buriticá et al., 2019). Recent work shows that inherited (Carboniferous) crustal-scale boundaries are preserved within the arc (Andico et al., 2017; Klepeis et al., 2019a) and have concentrated both Early Cretaceous magmatism and deformation. Importantly, structures and intrusions originating from different paleodepths are exposed at the surface along these boundaries due to the tilted nature of the section and extensive Cenozoic reverse faulting (e.g., Klepeis et al., 2019a, 2019b), making the area ideal for tracking the migration of deformation within the crustal column and for establishing temporal relationships between deformation and magmatism.

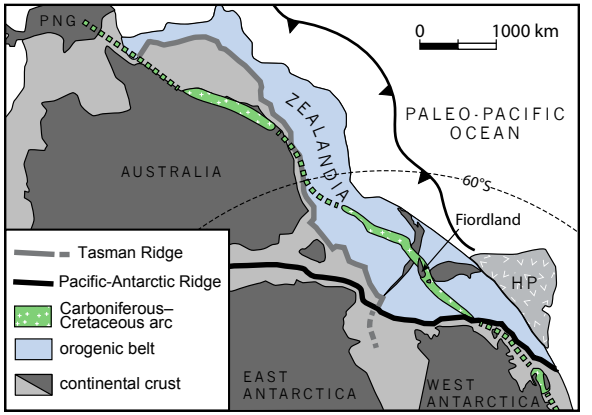

Figure 1. Tectonic reconstruction of Zealandia at ca. 90 Ma, including the Carboniferous–Cretaceous arc, orogenic belt, and continental crust (after Klepeis et al., 2016; modified from Mortimer, 2008). Location of Fiordland shown within arc. HP—Hikurangi Plateau; PNG—Papua New Guinea.

Within central Fiordland, we identified high-strain domains and reconstructed the pre-Cenozoic (pre-faulting) configuration of the crustal section. We then used observations of microstructures in thin section, trace-element thermometry, and U-Pb zircon and titanite geochronology to track the migration of deformation from lower- to middle-crustal levels within an inherited boundary in the Early Cretaceous Fiordland arc. These techniques allowed us to make connections between spatio-temporal patterns of transpressional deformation and the records of pluton crystallization and elevated mid-crustal temperatures. We evaluate these results in the context of the reactivated crustal-scale boundary and present them using a new series of geologic maps and cross sections. We document a four-phase deformation history spanning pre-WFO arc structure (D_1) through Miocene brittle to semi-brittle faulting (D_4); the latter of which contributed to the current juxtaposition of middle- and lower-crustal exposures. This work adds to the current record of transpressional

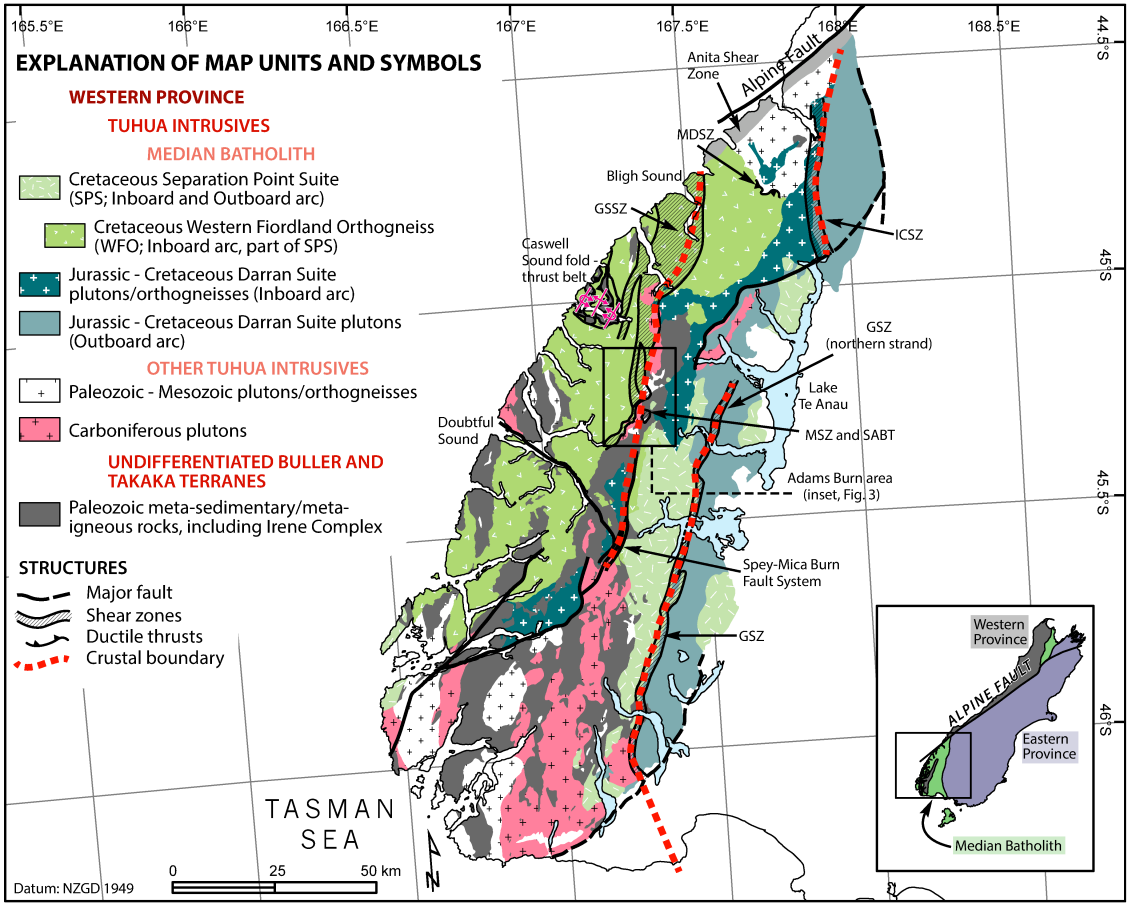

Figure 2. Simplified geologic map of Fiordland highlighting Cretaceous convergent-transpressional structures. Paleozoic crustal boundaries (after Klepeis et al., 2019a) are demarcated by red dashed lines, and the western boundary discussed in this study coincides with a linear belt of Carboniferous plutons, shown in pink. White-colored polygons immediately west of Lake Te Anau and near the south coast are Late Cretaceous–Cenozoic sedimentary cover rocks. Structures include the Caswell fold and thrust belt, the George Sound shear zone (GSSZ), the Grebe shear zone (GSZ), the Indecision Creek shear zone (ICSZ), the Misty shear zone (MSZ), the Mount Daniel shear zone (MDSZ), and South Adams Burn thrust (SABT). The study area is outlined at center. Lithologic contacts from GIS database of Turnbull et al. (2010). Inset after Allibone et al. (2009b). Colors of headings and indentations in the Explanation of map units reflect the tectonostratigraphic and igneous hierarchy of Fiordland's bedrock geology.

deformation in Fiordland and highlights the influence of structural inheritance on deformation and arc magmatism.

GEOLOGIC HISTORY AND PREVIOUS WORK

Magmatism

Fiordland preserves a long history of magmatism and deformation during arc construction along the Paleozoic to Cretaceous margin of Gondwana. Mesozoic arc magmatism, crustal thickening, and extensional orogenic collapse in Fiordland are preserved in Paleozoic metasedimentary and meta-igneous rocks. This package of Paleozoic to Mesozoic rocks is collectively referred to as the Western Province and includes the Early Paleozoic metasedimentary Buller and Takaka terranes (Fig. 2; Mortimer, 2004, and references therein). The neighboring Eastern Province is composed of Late Paleozoic–Mesozoic accreted terranes (Fig. 2; Mortimer, 2004, and references therein). The Tuhua Intrusives (Mortimer et al., 2014) encompass all igneous rocks of the Western Province, including the ~10,200 km^2 Mesozoic Median Batholith (Mortimer et al., 1999), and in Fiordland, is divided into an outboard (trenchward) and inboard (continentward) arc (Fig. 2; Turnbull et al., 2010). In the study area (Fig. 3), Tuhua Intrusives intrude metasedimentary rocks of the Irene Complex (Turnbull et al., 2010), including quartzofeldspathic gneisses, psammitic to pelitic gneisses and schists, and marble and calc-silicate horizons (Scott and Cooper, 2006).

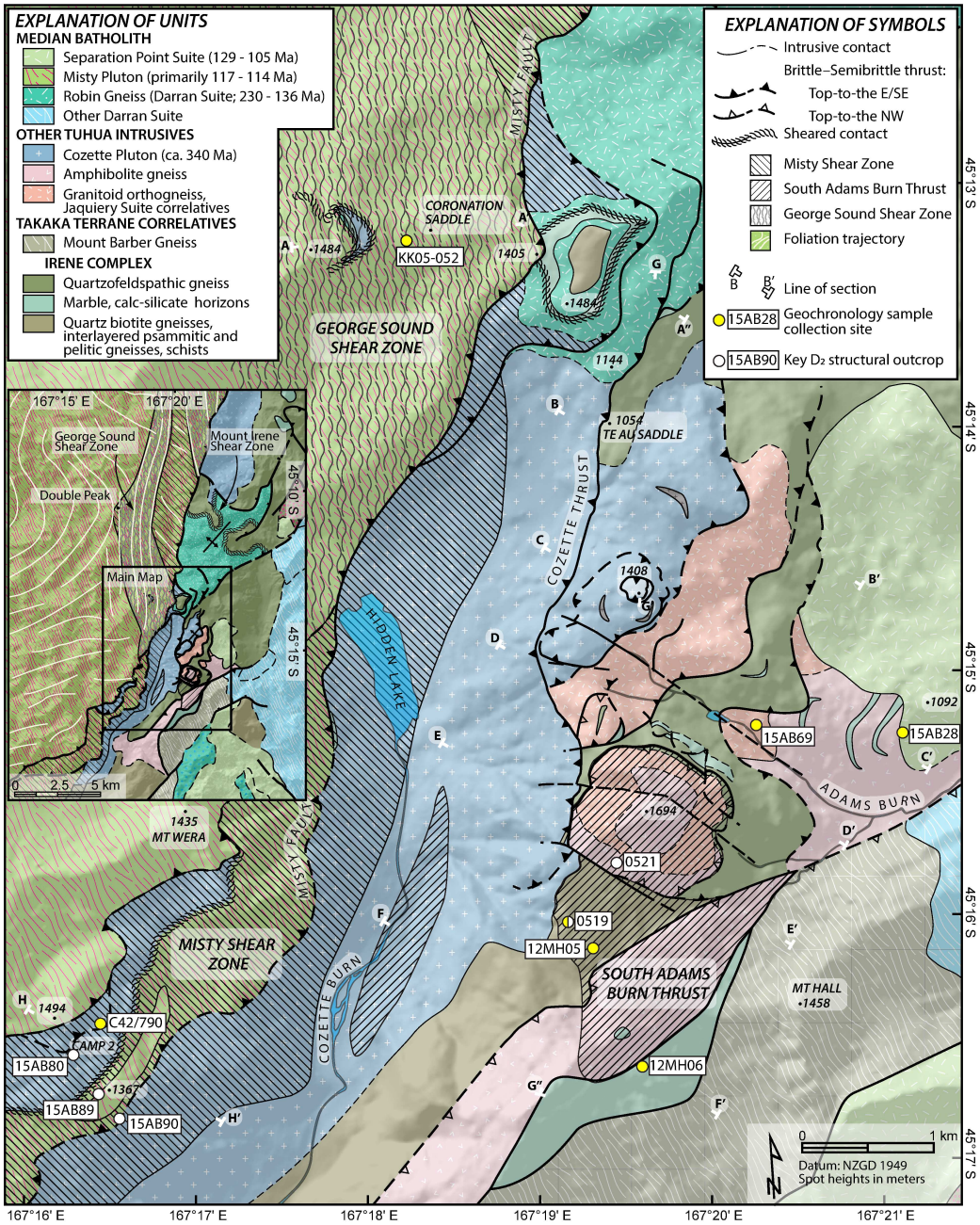

Figure 3. Geologic map of study area highlighting D_2-associated structures. Geochronology sample locations and key outcrops are noted. All generations of foliations, lineations, folds, and faults are represented in Supplemental Figure S1 (text footnote 1). Geology of the inset map and peripheral areas of the main map is based on Turnbull et al. (2010). The Irene Complex, as defined by Turnbull et al. (2010), includes granitoid orthogneiss and amphibolites. Where possible, we have separated these out as "Tuhua Intrusives," including amphibolite gneiss with a probable dioritic protolith. Outside of the main map area, the blue-green–colored map unit with blue crosses to the south is the Omaki Orthogneiss, and the blue-colored map unit with white crosses to the north is the Carboniferous Large Pluton.

The earliest magmatism associated with the Median Batholith is represented by several mainly short-lived events of Cambrian to Carboniferous age, with magmas intruded along the inboard portion of the arc (Ireland and Gibson, 1998; Allibone et al., 2007; Daczko et al., 2009; Tulloch et al., 2009; Turnbull et al., 2010; Turnbull et al., 2016). In the study area, this magmatism is represented by Early Paleozoic granitoid gneiss and dioritic amphibolite gneiss, followed by the Cozette Pluton (Fig. 3), an equigranular biotite ± garnet granite (Allibone et al., 2009a) with a crystallization age of ca. 340 Ma (Ramezani and Tulloch, 2009).

The next major episode of Median Batholith magmatism occurred between ca. 230 and 136 Ma with emplacement of Darran Suite plutons (Fig. 2) into the outboard component of the arc (Kimbrough et al., 1994; Tulloch and Kimbrough, 2003; Scott and Palin, 2008; Allibone et al., 2009a; Scott et al., 2009c; Schwartz et al., 2017). After a short hiatus in magmatism, the Separation Point Suite (SPS) magmatic flare-up event occurred between 129 and 105 Ma, with magmas emplaced at all crustal levels in the inboard and outboard sections of the arc (Tulloch and Kimbrough, 2003; Schwartz et al., 2017; Buriticá et al., 2019). The lower-crustal component of the SPS is the ~2300 km^2 Western Fiordland Orthogneiss (WFO) (Allibone et al., 2009b; Turnbull et al., 2010), emplaced at pressures between 1.0 and 1.8 GPa (Bradshaw, 1989; Clarke et al., 2000; Allibone et al., 2009b; Allibone et al., 2009c; Daczko et al., 2009; De Paoli et al., 2009), between ca. 128 and ca. 114 Ma (primarily from 118 to 115 Ma; Schwartz et al., 2017). The study area (Fig. 3) contains a small pluton of tonalitic middle-crustal SPS and lower-crustal hornblende dioritic rocks of the Misty Pluton (WFO) (Fig. 2); this pluton was emplaced in the study area as a subhorizontal, tabular intrusive.

Cretaceous Structures

Emplacement of Separation Point Suite plutons, including the WFO, coincided with sinistral transpression (Fig. 2; Klepeis et al., 2004; Allibone et al., 2010; Scott et al., 2011; Schwartz et al., 2017; Buriticá et al., 2019). Recognized syn-magmatic structures include the Mount Daniel shear zone, which formed during and after emplacement of the 124.0–121.8 Ma Worsley Pluton (Klepeis et al., 2004; Schwartz et al., 2017), and the 129–110 Ma Grebe shear zone (GSZ) (Fig. 2; Allibone et al., 2010; Scott et al., 2011; Buriticá et al., 2019). Post-WFO emplacement shear zones include the 119–111 Ma Indecision Creek (ICSZ) and George Sound (GSSZ) shear zones (Klepeis et al., 2004; Marcotte et al., 2005) and the 117–113 Ma Caswell fold and thrust belt (Fig. 2, Daczko et al., 2002; Klepeis et al., 2004; Schwartz et al., 2016). Collectively, these structures indicate that transpressional deformation at lower- and mid-crustal levels accompanied and outlasted the Early Cretaceous magmatism. These structures predate extensional shear zones that formed between 108 and 106 Ma (Klepeis et al., 2007; Klepeis et al., 2016; Schwartz et al., 2016).

Several of the transpressional and/or compressional structures outlined above are located along crustal-scale boundaries in Fiordland. The GSZ and ICSZ mark the boundary of the inboard and outboard arcs (Marcotte et al., 2005; Allibone et al., 2009b; Scott et al., 2011; Buriticá et al., 2019). The Cretaceous GSSZ coincides with an ~5-km-wide, linear belt of Carboniferous granitoid plutons that includes the Cozette Pluton (Ramezani and Tulloch, 2009; Allibone et al., 2009a, and references therein; Turnbull et al., 2010). Andico et al. (2017) identified sharp $\delta^{18}O$ gradients within suites of Jurassic plutons spatially associated with the linear belt of Carboniferous plutons, and they found the observed gradient to be consistent with intrusion into a Jurassic or older suture. Decker et al. (2017) showed that the Early Cretaceous WFO plutons, emplaced in the lower crust adjacent to the linear belt of Carboniferous plutons, have zircon isotopic compositions that indicate a mantle source. Furthermore, the linear belt of Carboniferous plutons coincides with the boundary between Cretaceous mid- and lower-crustal blocks illustrated by Klepeis et al. (2019a). The patterns described above are all consistent with a persistent, crustal-scale structure in Fiordland (Klepeis et al., 2019a).

Cenozoic Faulting

Cenozoic brittle faulting has reorganized Fiordland's Cretaceous crustal blocks. These brittle features record the Eocene–Miocene transition from transtensional to transpressional deformation linked to the initiation of subduction and formation of the Alpine fault (King, 2000; Lebrun et al., 2003; Furlong and Kamp, 2009). Faults also record increased uplift (Sutherland et al., 2009) owing to the interaction between the subducted portions of the Hikurangi Plateau and Pacific plate beneath Fiordland (Klepeis et al., 2019a). In the study area, these features are part of the Misty fault segment (Klepeis et al., 2019a; Klepeis et al., 2019b), a reactivated northern extension of the Spey-Mica Burn fault system (Fig. 2). Miocene faults in the study area are important because they juxtaposed Cretaceous lower- and mid-crustal structures and are used to reconstruct the Early Cretaceous crustal structure.

METHODS

Field Mapping and Sampling

We constructed a lithologic and structural map (Fig. 3 and Supplemental Fig. S1[1]) covering the pluton–host rock contacts of the Misty and Cozette Plutons and a significant portion of the Irene Complex adjacent to the Cozette Pluton. Cross sections and a terrain model (Figs. 4 and 5; Supplemental Fig. S1) reveal the 3-D geometry of structures, particularly two Early Cretaceous shear zones. Standard field-mapping techniques, including observation of cross-cutting relationships, kinematic indicators, and description of igneous and metamorphic fabrics, allowed us to identify an early foliation (S_1) formed prior to emplacement of the Cozette Pluton (D_1) and two Cretaceous shear zones formed approximately coeval with emplacement of Western Fiordland

GSA Data Repository item #

Citation goes here

LIST OF FILES

Supplemental Text: Detailed description of geochronology methods

Table S1: GPS locations of samples used for geochronological analyses
Table S2: U-Pb zircon SHRIMP-RG isotopic data and ages
Table S3: Zircon SHRIMP-RG trace element and geochemical data
Table S4: U-Pb zircon LA-MC-ICP-MS isotopic data and ages
Table S5: U-Pb titanite LA-MC-ICP-MS isotopic data and ages
Table S6: Titanite LA-Q-ICP-MS trace element data and temperatures for sample 12MH06.

Figure S1: Detailed structural and lithologic map and cross sections of field area
Figure S2: Scanning electron microscope cathodoluminescence images of analyzed zircon grains in samples (A) 12MH05, (B) C42/790, (C) 15AB69, (D) 15AB28.
Figure S3: Representative scanning electron microscope cathodoluminescence images of zircon grains in samples (A) 0519A, (B) 0519G.
Figure S4: Scanning electron microscope back-scattered electron images of analyzed titanite grains in sample 12MH06.

DETAILED DESCRIPTION OF GEOCHRONOLOGY METHODS

U-Pb zircon geochronology and geochemistry analyses were completed using an ion microprobe at the Stanford-USGS SHRIMP-RG facility (Supplementary Tables S2, S3), and with laser ablation multicollector inductively coupled plasma mass spectrometry (LA-MC-ICP-MS) at the Arizona LaserChron Center (Supplementary Table S4). U-Pb titanite thermochronology and geochemistry analyses were completed with laser ablation split-stream inductively couple plasma mass spectrometry (LASS-ICP-MS) at the University of California – Santa Barbara laser ablation split stream facility (Supplementary Tables S5, S6).

SHRIMP-RG Geochronology Methods

U-Pb zircon geochronology data were collected at the USGS-Stanford Ion Microprobe Laboratory at Stanford University, California (Bacon et al., 2012). Two mounts were analyzed during two different analytical sessions: mount 15CSUN59, analyzed March 5th, 2015, and mount 15CSUN77, analyzed October 15th, 2015. Zircon geochronology standards R33 (419 Ma quartz diorite zircon; Black et al., 2014) and Stanford in-house compositional standard, MADDER, were added to both mounts. Each mount contains zircon grains initially concentrated using standard heavy mineral separation processes, hand-picked for final purity, and aligned in 1 x 6 mm rows on double-sided tape. The tape was adhered to a glass slide and then cast in 25 mm diameter by 4 mm thick epoxy discs (the mounts). The epoxy discs were ground and polished to a 1 µm finish, washed with a 1 N HCl solution, rinsed with distilled water, and dried in a vacuum oven.

[1]Supplemental Material. Analytical methods used are described in Supplemental Text. Sample collection locations shown in Figure 3 are detailed in Table S1. Isotopic and geochemical data for zircon analyses are presented in Tables S2–S4. U-Pb isotope data and geochemistry data for titanite analyses are presented inTables S5 and S6, respectively. A series of cross sections and a geologic map of the study area including field stations and associated structural measurements are presented in Figure S1. Cathodoluminescence images of zircon grains are shown in Figures S2 and S3. Backscattered electron images of analyzed titanite grains are presented in Figure S4. Please visit https://doi.org/10.1130/GEOS.S.12728606 to access the supplemental material, and contact editing@geosociety.org with any questions.

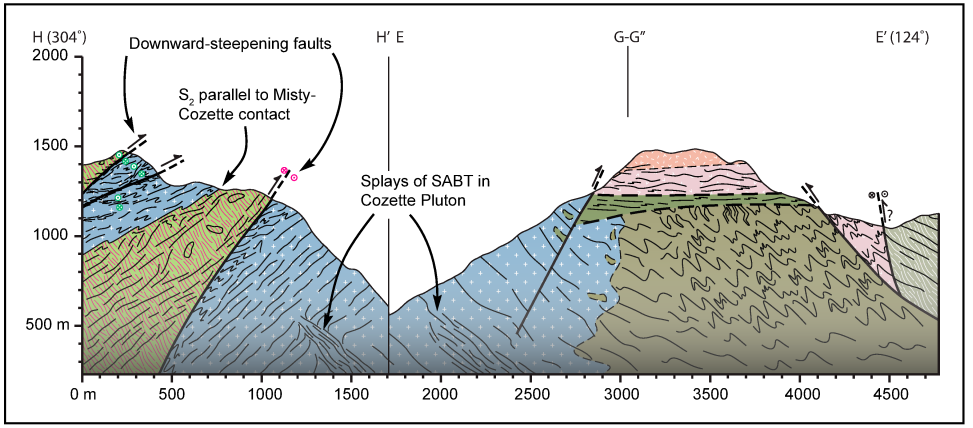

Figure 4. Composite cross section H–H′ and E–E′. Extent of cross section is denoted in Figure 3 and integrated with block diagram in Figure 5. The profile highlights the downward-steepening faults that accommodated significant Miocene vertical displacements and could not have substantially rotated Cretaceous structures. Refer to Figure 3 for legend. SABT—South Adams Burn Thrust.

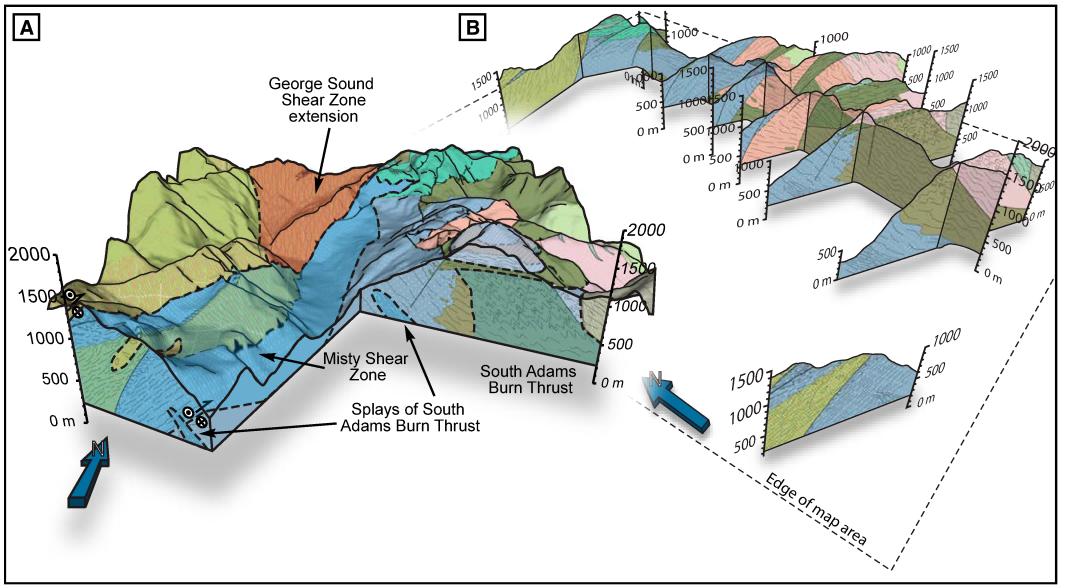

Figure 5. Reconstructions of Cretaceous shear zones and overprinting faults in the study area, with no vertical exaggeration. (A) Perspective terrain model and geologic map of the field area highlighting the distribution, geometry, and kinematics of major Early Cretaceous shear zones in the Misty Pluton and its host rock, including the Misty shear zone (MSZ) and South Adams Burn Thrust (SABT). Terrain data from GIS database of Turnbull et al. (2010). Geologic contacts from Figure 3. Cross sections from B, this figure. (B) Perspective fence diagram emphasizing the distribution and geometry of overprinting brittle–semi-brittle faults that juxtapose Cretaceous structures at the same crustal level. Profiles correspond to data from Figure 3. Individual profiles included in Supplemental Figure S1 (text footnote 1).

Orthogneiss and Separation Point Suite plutons (D_2). Timing of D_2 relative to magmatism was determined using U-Pb zircon geochronology of intrusives and variably crosscutting dikes. Field mapping also allowed us to delineate two distinct rock units originally described as part of the Irene Complex (an amphibolite gneiss of probable dioritic origin and a granitoid gneiss) and shown as Tuhua Intrusives in Figure 2. We focus on description of two Cretaceous structures associated with D_2, the Misty shear zone and South Adams Burn thrust (Figs. 6 and 7). Structures associated with two subsequent deformation events (D_3 and D_4) are used to reconstruct the relative positions of the Cretaceous lower- and middle-crustal exposures.

Zircon Geochronology

We analyzed zircons from plutonic units and syn- and post-tectonic dikes to determine the timing of D_2-associated deformation and melt crystallization. One plutonic unit (sample 15AB28) and four dikes (samples C42/790, 12MH05, 15AB69, and 12MH06A) were analyzed using the U.S. Geological Survey (USGS)–Stanford University sensitive high-resolution ion microprobe with reverse geometry (SHRIMP-RG). Two felsic dike samples (0519A and 0519G) were analyzed at the University of Arizona LaserChron Center by laser ablation–inductively coupled plasma mass spectrometry (LA-ICP MS). We present all $^{206}Pb/^{238}U$ ages as weighted means with 2σ standard error and mean square of weighted deviates (MSWD) when reporting inferred crystallization ages. Analyses omitted from calculated weighted-mean ages are represented in concordia diagrams for reference. Sample collection locations are shown in Figure 3 and detailed in Supplemental Table S1. Isotopic and geochemical data are presented in Supplemental Tables S2–S4. Descriptions of analytical methods are presented in supplemental text, and cathodoluminescence (CL) images of zircon grains are shown in Supplemental Figures S2 and S3.

Titanite Thermochronology and Trace-Element Thermometry

To investigate the record of continued thermal activity following D_2, we completed U-Pb titanite thermochronology analyses of a calc-silicate sample collected from the Irene Complex south of point 1694 m (sample 12MH06, Fig. 3). Titanite was analyzed at the University of California Santa Barbara laser ablation split stream petrochronology facility, using laser ablation split stream–inductively coupled plasma mass spectrometry (LASS-ICP MS). U-Pb isotope data and geochemistry data for the sample are presented in Supplemental Tables S5 and S6 (footnote 1), respectively. Backscattered electron images of analyzed titanite grains are presented in Supplemental Figure S4. Geographic coordinates of the sample collection location are contained in Supplemental Table S1, and analytical methods used are described in the Supplemental Text.

Zr-in-titanite temperatures were calculated using Zr concentrations measured for the same spots as U-Pb isotopic concentrations, allowing for comparison of dates and temperatures during titanite (re)crystallization. Temperatures were calculated using the calibration of Hayden et al. (2008), assuming P = 0.8 GPa, $a\mathrm{TiO_2} = 1$, and $a\mathrm{SiO_2} = 1$. The chosen pressure of 0.8 GPa reflects the location of the sample within the middle crust during the Early Cretaceous. Because rutile is not present in this sample, we set $a\mathrm{TiO_2}$ at unity to represent an upper limit of calculated temperatures. Analytical uncertainties associated with Zr measurements range between 4% and 15% (2σ SE [standard error]), resulting in errors in calculated temperatures up to 8 °C. We take a more conservative estimate of ±15 °C, although this does not account for uncertainties in pressure at the time of titanite (re)crystallization.

RESULTS

Structural Geology and Relative Chronology of Deformation Events

Paleozoic Units and Deformation (D_1)

Host rock of the Cozette Pluton (Irene Complex and older Tuhua Intrusives) preserves a penetrative gneissic foliation (e.g., Fig. 7A) parallel to the large-scale lithologic layering characteristic of the units. Layers of quartzofeldspathic gneisses, pelitic schists, marbles, and amphibolites are each tens to hundreds of meters thick. S_1 is primarily defined by a preferred orientation of hornblende or biotite grains (Figs. 7A and 7B). In some garnet-bearing lithologies, an internal foliation of inclusion trails discontinuous with the matrix foliation is preserved (e.g., Fig. 7C), highlighting the composite nature of S_1. In many portions of the study area, S_1 was overprinted during a second deformation event (D_2, described below). The gneissic S_1 composite foliation is the oldest observed structure in the study area and is not observed within the Cozette Pluton. Therefore, we infer that S_1 formed prior to emplacement of the Cozette Pluton.

Misty Shear Zone (D_2)

Along the contact between the Misty and Cozette Plutons, parallel subsolidus gneissic and suprasolidus magmatic fabrics record approximately arc-parallel displacements during intrusion of the Misty Pluton, a part of the ca. 128–114 Ma WFO. For reference, the majority of the Misty Pluton was emplaced between 117 and 114 Ma (Schwartz et al., 2017), with some portions, including the area of our study site, crystallized as early as ca. 123 Ma (Allibone et al., 2009b). We name the newly identified structure the Misty shear zone (MSZ; Figs. 3 and 5). The "type locality" for the MSZ is in the SW portion of the field area at Camp 2 (Fig. 3). In the Misty Pluton at Camp 2, the foliation is recognized by aligned mm-thick hornblende- and plagioclase-rich domains. This foliation contains a lineation defined by elongate hornblende aggregates and aligned biotite and plagioclase grains. In thin section, plagioclase commonly exhibits growth twins and displays largely straight grain boundaries with no

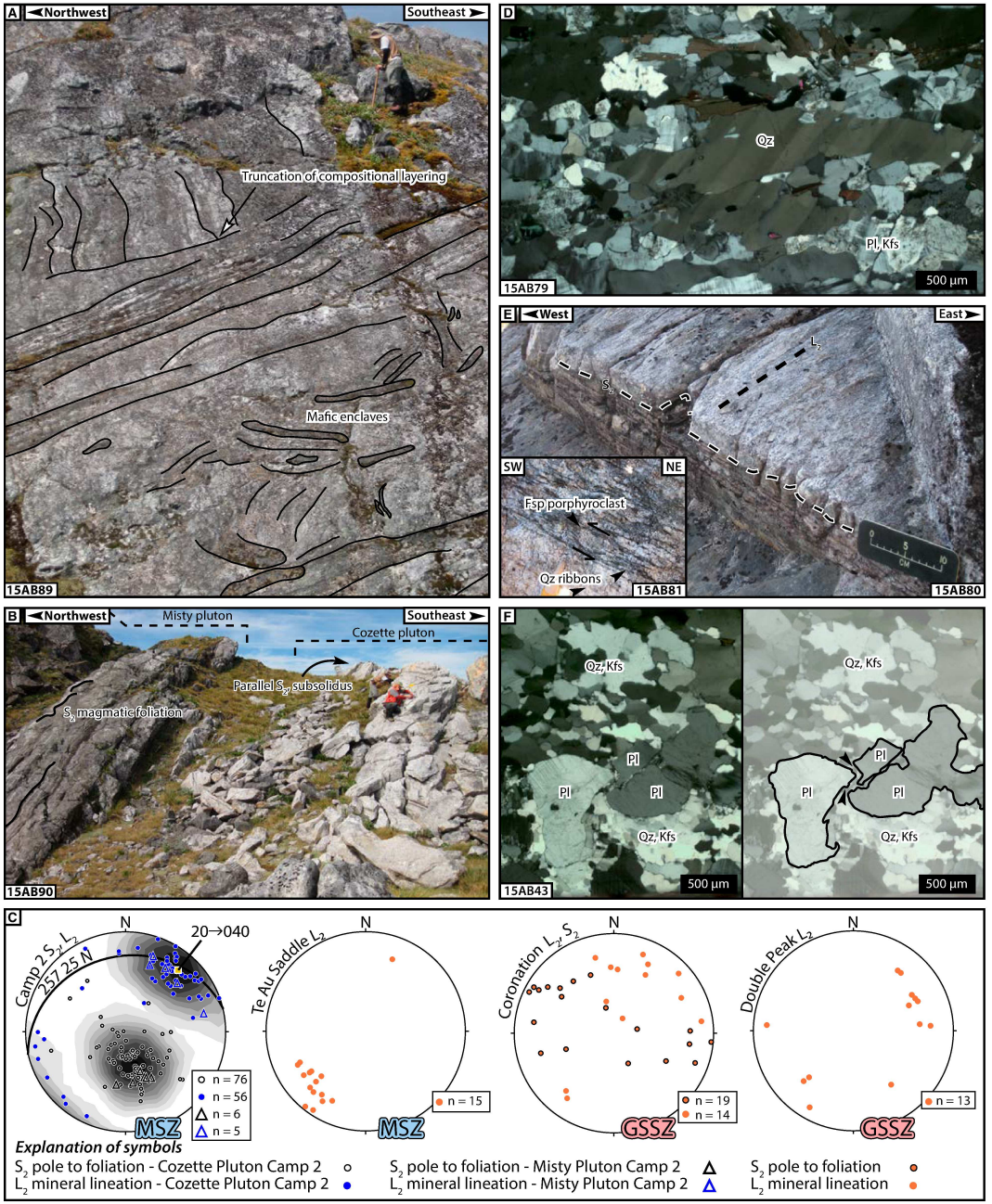

Figure 6. Outcrop, thin-section, and geometric characteristics of oblique sinistral-reverse shear zone (MSZ—Misty shear zone) along the margin of the Misty Pluton. (A) Evidence of suprasolidus deformation in the Misty Pluton at Camp 2. This outcrop is outside of the domain extensively deformed by the MSZ and shows compositional layering truncated by other compositional layering. With no evidence for solid-state structures, this relationship is consistent with suprasolidus deformation. (B) Parallelism of magmatic fabric in the Misty Pluton and Gneissic S_2 in Cozette Pluton. This relationship indicates coeval shearing and Misty Pluton emplacement. (C) Lower-hemisphere, equal-area stereonet structural summaries of locations with pronounced S_2 and L_2 north and west of Cozette Burn. Left-most stereonet shows parallelism of both foliation and lineation in the Misty and Cozette Plutons along the Misty-Cozette sheared contact, at the type locality of the MSZ. Te Au saddle stereonet presents Cozette Pluton fabrics that we correlate with the MSZ east of the Cenozoic Misty fault. Other stereonets highlight subsolidus fabrics that we correlate with the George Sound shear zone (GSSZ). (D) Thin-section photomicrograph (cross-polarized light) of D_2-associated Misty shear zone textures in Cozette Pluton, ~200 m from contact with the Misty Pluton. Large, mm-thick quartz ribbons define the gneissic foliation. Sample cut parallel to macroscopic lineation and perpendicular to macroscopic foliation. (E) Gneissic S_2 and L_2 associated with the MSZ in the Cozette Pluton. Occasionally, feldspar (Fsp) porphyroclasts display asymmetric sigmoidal tails indicating a top-to-the-southwest sense of shear (Inset). (F) Thin-section photomicrograph (cross-polarized light) of textures suggestive of former melt in Cozette Pluton on East side of Cozette Burn, ~2 km from contact with Misty Pluton. Plagioclase grains invariably have highly irregular grain boundaries, typically with low dihedral angles in contact with quartz-rich and potassium feldspar–rich domains, highlighted with arrows in sketch. This sample contains no observable macroscopic fabric. Locations of field stations (e.g., 15AB89) are provided on the supplemental map of Figure S1 (text footnote 1).

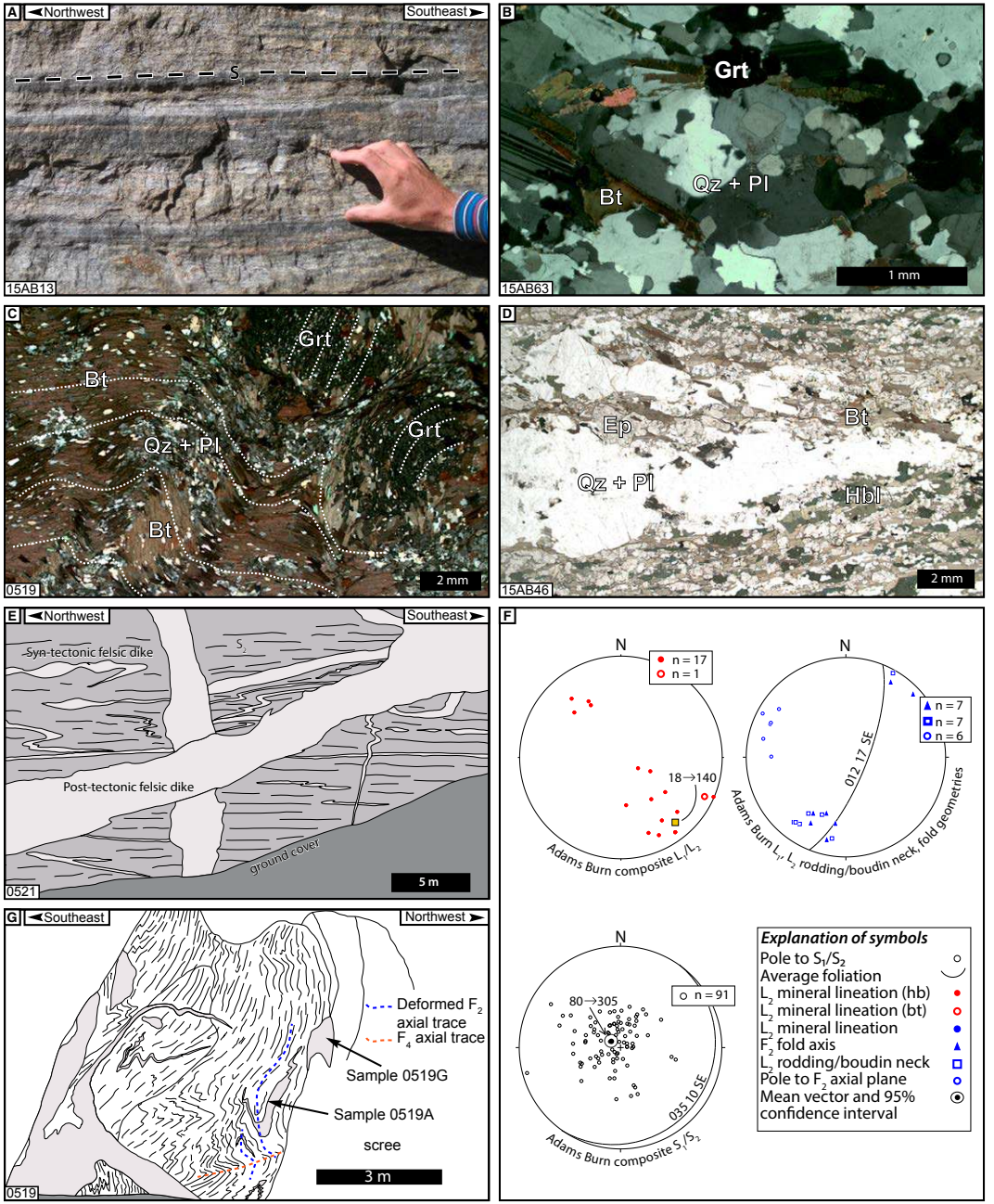

Figure 7. Outcrop, thin-section, and geometric characteristics of S_1, and of the South Adams Burn thrust (SABT) in the Irene Complex and older Tuhua Intrusives. (A) Outcrop photograph of quartzofeldspathic gneiss within the Irene Complex, displaying an S_1 composite foliation, defined by compositional layering of more mafic and felsic layers. (B) Thin-section photomicrograph of S_1 in a quartzofeldspathic gneiss. Biotite defines the foliation but is more pronounced in outcrop. (C) Thin-section photomicrograph (cross-polarized light) of folding associated with the SABT. Sample collected from the same outcrop represented in E. Dashed lines highlight inclusion trails in garnet and crenulated S_1. (D) Thin-section photomicrograph of foliation associated with the SABT. Hornblende, biotite, and elongate quartz-rich and feldspar-rich domains define the foliation in this sample. Sample collected 200 m west of amphibolite outcrop shown in E along the same cliff face. (E) Outcrop sketch of gently dipping South Adams Burn thrust zone on southern slope of pt. 1694 m. Plane of outcrop contains the L_2 mineral-stretching lineation and is coplanar with the plane of maximum asymmetry. (F) Lower-hemisphere, equal-area stereonet structural summaries of D_2-associated structures in the Irene Complex and older Tuhua Intrusives east of Cozette Burn (South Adams Burn thrust). (G) Outcrop sketch of NW-vergent folds associated with the SABT south of pt. 1694 m at station 0519. Collection locations of geochronology samples 0519A and 0519G (described in text) shown. Locations of field stations (e.g., 15AB13) are provided on the supplemental map of Figure S1 (text footnote 1).

signs of internal strain or recrystallization microstructures such as subgrains. Individual hornblende grains within aggregates also display straight grain boundaries and commonly contain quartz inclusions. Biotite is present as well-formed laths that do not occur as strain shadows around other phases. These characteristics are consistent with features of magmatic fabrics summarized by Paterson et al. (1998). At the outcrop scale, the Misty Pluton at Camp 2 preserves tiled mafic to ultramafic enclaves, and decimeter-scale compositional layering (Fig. 6A). Layers range from amphibolitic to dioritic to more leucocratic and plagioclase-rich. In portions of the Misty Pluton that do not show a uniform, pervasive magmatic foliation (Fig. 4), this compositional layering is truncated by other sets of compositional layering and displays no textures associated with subsolidus faulting or shearing (Fig. 6A), suggesting that deformation occurred in the presence of melt.

At the contact between the Misty and Cozette Plutons near point 1367 m (Fig. 3), the Misty Pluton magmatic foliation and lineation is co-planar and co-linear, respectively, with a gneissic foliation and lineation in the Cozette Pluton (Figs. 6B and 6C). The gneissic foliation in the Cozette Pluton is defined by mm-thick quartz ribbons that are interlayered with plagioclase + potassium feldspar + biotite-rich domains (Fig. 6D). The corresponding lineation near points 1494 m and 1367 m (Fig. 3) is defined by elongate quartz ribbons and biotite aggregates (Fig. 6E). The contact between the Misty and Cozette Plutons parallels S_2 (Fig. 4).

In both rock units at Camp 2 (Fig. 3), S_2 dips gently to moderately to the north (average S_2: 257, 25 N), and L_2 mineral lineations trend northeast-southwest, primarily plunging to the northeast (average L_2: 20 > 040; Fig. 6C). In the Cozette Pluton, sigmoidal feldspar porphyroclasts (inset in Fig. 6E) identified at four stations suggest top-to-the-SW sense of shear, indicating that deformation was oblique sinistral reverse. Parallelism between S_2 and L_2 in the Cozette and Misty Plutons, and the suprasolidus nature of the structures in the latter, suggest that oblique sinistral-reverse shearing occurred during emplacement of the Misty Pluton. Relative timing of deformation at Camp 2 is bracketed by the emplacement of the Misty Pluton and by an unfoliated leucocratic dike that crosscuts S_2- and L_2-bearing Cozette Pluton. U-Pb zircon geochronology results of this latter sample are presented in the zircon geochronology section.

Other exposures of the Misty Pluton along its margin display entirely subsolidus textures. North of Camp 2 near Coronation saddle (Fig. 3), the Misty Pluton displays subsolidus NE-SW–trending mineral lineations (Fig. 6C), typically defined by elongate hornblende and/or biotite. Elongate hornblende and plagioclase aggregates define a NE-SW–trending mineral lineation farther north at Double Peak (Fig. 3 Inset; Fig. 6C). Foliation and lineation at these locations are less uniform than at Camp 2, but L_2 has broadly the same NE-SW trend. S_2 variability may be the result of changing strain geometry during the transition to subsolidus deformation or extensive modification by younger structures.

At Te Au saddle, D_4-associated reverse faults bound multiple thrust slices preserving S_2 and L_2 structures that we interpret to be equivalent to those at Camp 2 (Fig. 3). The Cozette Pluton in this part of the map area displays the same gneissic foliation with mm-thick quartz ribbons and quartz + biotite lineation as is present at Camp 2. These exposures are found in the footwall of a major Cenozoic reverse fault (Misty fault; see Klepeis et al., 2019b). However, the portions of this fabric mapped east of the Misty fault in the Cozette Pluton in Figure 3 represent a minimum extent. Probable correlative fabrics are present in the Irene Complex and Robin Gneiss adjacent to the Cozette Pluton, but their extents have not been determined.

Mineral lineations along the eastern margin of the Misty Pluton and in its host rocks have a shared composition and geometry and are the oldest observed fabric in the Misty Pluton in the field area. Combined geometry and kinematic data indicate that the MSZ is an oblique sinistral-reverse shear zone. A conservative estimate of MSZ extent takes the western boundary to be immediately west of Camp 2, extending north until it is overprinted by the southern extent of the subsolidus GSSZ. The eastern extent of the MSZ is unclear due to imbricated thrust slices (minimum extent shown in Fig. 3). East of Cozette Burn, outcrops of the Cozette Pluton's eastern margin are variably foliated but do not show the characteristic north-dipping foliation of the MSZ. Weakly foliated outcrops east of Cozette Burn commonly contain microstructures consistent with the presence of former partial melt (Fig. 6F), including irregularly shaped plagioclase grains in a matrix of quartz and potassium feldspar and low dihedral angles between plagioclase and quartz + potassium feldspar domains. This suggests that the thermal aureole of the Misty Pluton extended beyond the footprint of the MSZ. We therefore take the lower boundary of the MSZ to be east of Camp 2 on the western slopes of the valley approaching Cozette Burn. Using an average foliation dip of 25° yields a minimum MSZ thickness estimate of ~614 m above the Misty Thrust and ~597 m below the Misty Thrust at Camp 2, where the extent of the MSZ is best constrained (Fig. 3).

South Adams Burn Thrust (D_2)

East of the contacts between the Irene Complex, older Tuhua Intrusives, and the Cozette Pluton (Fig. 3), a series of ductile structures associated with NW-SE–directed shortening occurs within amphibolites and quartzofeldspathic gneisses and schists of the Irene Complex and older Tuhua Intrusives. These structures form the newly identified South Adams Burn thrust (SABT; Figs. 3 and 5). In amphibolite exposures south of point 1694 m (Fig. 3), a gently SE-dipping gneissic foliation is defined by aligned hornblende, biotite, and euhedral epidote grains, and by alignment of boudinaged felsic veins and dikes (Figs. 7D and 7E). Necks of boudins trend SW (Fig. 7F). Synkinematic biotite is present in strain shadows of intergrown epidote and hornblende. The mineral lineation in this outcrop is defined primarily by aligned biotite grains, and less commonly by hornblende, and trends dominantly NW-SE (Fig. 7F).

Structurally below the amphibolite exposures of point 1694 m, quartzofeldspathic gneisses and schists display pervasive folding of an earlier foliation (Fig. 7G). The foliation in this area is primarily defined by biotite and contains foliation-parallel felsic veins, as is observed on the southern slopes of point 1694 m. Felsic veins (yielding Cretaceous U-Pb zircon ages; see geochronology

section) here are less extensively boudinaged, but the foliation is otherwise similar—interpreted to be S_1 modified during a second phase of deformation to produce a composite S_1/S_2 foliation. There is some evidence for biotite growth in strain shadows of garnet, but in this area, the modified S_1 is more extensively deformed by folding (Fig. 7C) than it is altered by growth of new foliation-defining minerals. S_1-defining biotite grains are crenulated and distorted around garnet porphyroclasts, which preserve an internal foliation as sets of curvilinear inclusion trails discontinuous with S_1 in the matrix (Fig. 7C). F_2 folds deform the composite foliation (Fig. 7G) and are steeply inclined, tight-isoclinal and NW-vergent, with SW-trending fold axes (Fig. 7F). This style of folding was observed at four field stations. In these outcrops, F_2 is refolded by a moderately inclined, NW-vergent F_4 (discussed below). Additionally, a SE-dipping gneissic foliation is locally developed in the Cozette Pluton on the eastern side of the valley containing Cozette Burn (Fig. 3). This contrasts strongly with the extensively recrystallized amphibolites on the southern face of point 1694 m.

The northwest vergence of F_2 folds and parallelism of fold axes and boudin necks suggests that the two structures (S_2/L_2 in the amphibolite outcrop and primarily F_2 in the structurally lower gneisses and schists) are kinematically compatible with NW-SE–directed shortening. Both the NW-SE–trending mineral lineation in the amphibolite and NW-vergent folds are consistent with top-to-the-NW sense of shear. The two structures share a fabric-defining mineral assemblage, are in close proximity to one another, and have common cross-cutting relationships with leucocratic dikes (Figs. 7E and 7G). Both "styles" of exposures contain synkinematic dikes as well as later dikes that crosscut the observed S_2 tectonic fabric and F_2 folds. U-Pb zircon geochronology results for both generations of felsic dikes are presented below. Together, these two styles of structures comprise what we term the South Adams Burn thrust (SABT). We conservatively delineate the extent of the SABT where S_2 and F_2 were observed east of Cozette Burn (Fig. 3), with an along-strike length of ~2 km, but it is likely that such structures extend farther to the east and south.

Late Shear Zones and Faults (D_3, D_4)

Shear zones and brittle faults formed during D_3 and D_4, respectively, and deform the MSZ and SABT. These late structures juxtapose lower- and middle-crustal exposures at the surface (Klepeis et al., 2019a), and an understanding of their architecture and kinematics is essential for interpreting the original configuration of the MSZ and SABT.

Locally, thin (<10 m) greenschist-facies mylonitic to ultramylonitic shear zones deform S_2 in the Cozette and Misty Plutons (Fig. 8A). S_3 is defined by cleavage domains of fine-grained biotite and microlithons of recrystallized feldspar and quartz. L_3 is defined by elongate aggregates of fine-grained biotite, feldspar, and quartz. S_3 dips moderately, with variable dip directions between NW and SW, although dominantly to the NW. L_3 plunges gently to the W-SW (see Fig. 2B of Klepeis et al., 2019b). S_2 foliation deflections, sigmoidal pods with intact S_2/L_2 structures, C′-type shear band cleavages, sigmoidal feldspar porphyroclasts with tails of chlorite or biotite, and inclined quartz subgrains all suggest top-to-the-W/SW displacement. This displacement indicates dominantly oblique-normal shearing with a sinistral component. These characteristics differ significantly from the more gneissic, D_2-associated structures.

Most lithologic contacts in the field area are brittle to semi-brittle faults (Fig. 3) that typically contain pseudotachylyte (e.g., Fig. 8B). Based on a combination of features including fault plane geometry, slickenlines, offset dikes, and stepped fault surfaces, we identified populations of reverse faults, oblique-reverse faults, and strike-slip faults. Reverse and oblique-reverse faults are most pronounced (Fig. 8C), with SE-NW– and E-W–trending shortening directions, respectively. Hanging walls are displaced top-to-the-southeast or top-to-the-east. These faults displaced the margin of the Misty Pluton to the same structural level as the Cozette Pluton, which in turn was displaced upward into adjacency with the Irene Complex (Fig. 3). We interpret movement along these faults to be a mechanism by which lower-crustal exposures (Misty Pluton) were brought to the same level as mid-crustal rocks (Cozette Pluton, Irene Complex) in the study area. These concave-down faults are steeply dipping (Figs. 4 and 5), and therefore could not have significantly modified the geometry of structures formed during D_2.

Footwalls of several faults display ductile structures that are kinematically compatible with the nearby faults. This is particularly true in exposures of the Irene Complex south of pt. 1694 m, where NW-vergent folds underlie one of the only identified top-to-the-NW reverse faults. Fold axes, boudin necks, and mineral lineations defined by low-grade phases such as chlorite are also compatible with top-to-the-northwest hanging-wall displacement. These F_4 folds overprint F_2 folds (Fig. 7G).

Zircon Geochronology

Misty Shear Zone

Sample C42/790 was collected from a >4-m-thick undeformed leucodiorite dike that crosscuts the MSZ in the Cozette Pluton at Camp 2 (Fig. 3). Most analyzed grains are subhedral, have a diameter >200 μm, and have CL-visible core and rim domains (Supplemental Fig. S2 [footnote 1]). SHRIMP-RG analysis of 17 total spots (cores and rims) on 17 grains yielded a weighted-mean $^{206}Pb/^{238}U$ age of 121.1 ± 1.7 Ma (MSWD = 3.8) after rejection of six analyses that yielded pre-WFO intrusion dates (Fig. 9A). Pre-WFO dates do not clearly correlate with position in grains. The MSWD of 3.8 for this sample suggests that the 11 analyzed grains comprise more than one population. To explore this, we calculated a weighted-mean $^{206}Pb/^{238}U$ age of the youngest five grains to be 117.8 ± 1.5 Ma (MSWD = 0.6) (Fig. 9B). The six older grains have a weighted-mean age of 122.3 ± 1.7 (MSWD = 1.9) and may represent a xenocrystic population originating from the Misty Pluton host rock of the sampled leucodiorite dike. We interpret the youngest five analyses to represent the crystallization age of the leucodiorite dike.

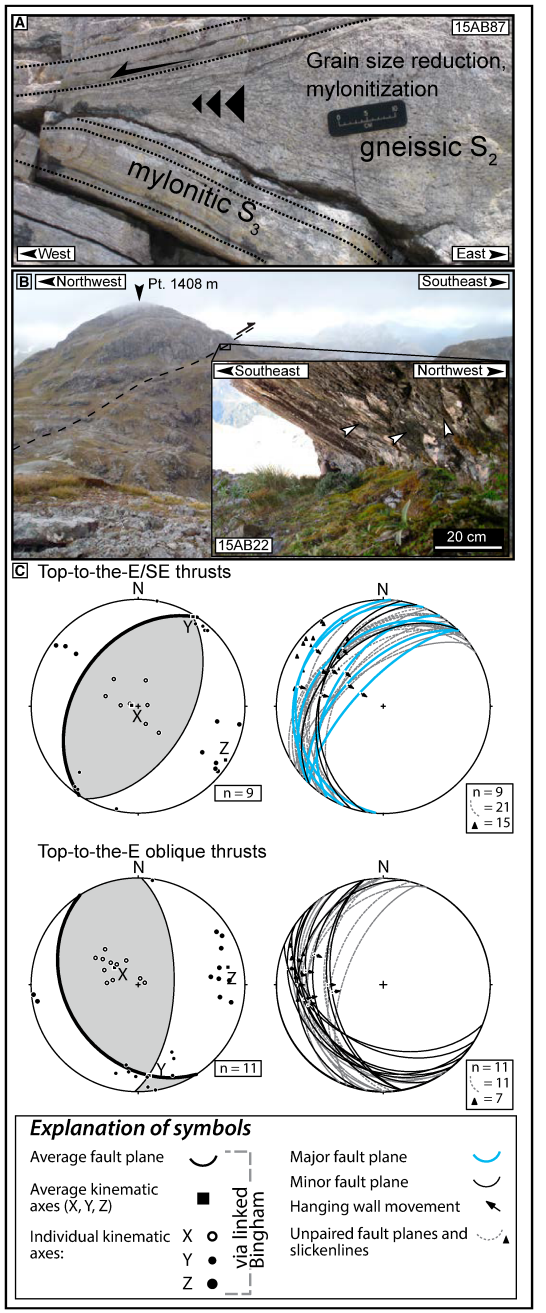

Figure 8. Summary of structures formed during D_3 and D_4. (A) Transposition of gneissic S_2 into late, mylonitic shear zone formed during D_3 near Camp 2 at station 15AB87 (field station location is provided on Fig. S1 [text footnote 1]). (B) Field photographs of a major top-to-the-SE thrust below pt. 1408 m (see Fig. 3 for map location). Areas of pseudotachylyte-bearing fault surface are indicated with arrows. Scale applies to image foreground. (C) Fault-plane solutions and fault-slip data for top-to-the-E/SE thrust faults, the most pronounced fault populations in the study area. After Klepeis et al. (2019b).

Previous geochronology work on a sample of the Misty Pluton from Coronation saddle (Fig. 3) (Allibone et al., 2009b) yielded a $^{206}Pb/^{238}U$ zircon crystallization age of 122.6 ± 1.9 Ma (2σ). This is close in age to the inferred xenocrystic population calculated for sample C42/790 and helps to bracket the timing of movement along the MSZ. The igneous S_2/L_2 in the Misty Pluton suggests that the MSZ was active during Misty Pluton emplacement, which occurred at ca. 123 Ma in the area immediately west of Adams Burn according to Allibone et al. (2009b). The leucodiorite dike crosscuts S_2/L_2 and is undeformed, indicating that the MSZ had ceased operating, at least locally, by ca. 118 Ma. The timing of MSZ initiation, if it was active prior to Misty Pluton emplacement, is not known.

South Adams Burn Thrust

Sample 0519A is a pre-tectonic, quartzofeldspathic dike collected from an outcrop of the Irene Complex south of point 1694 m (Figs. 3 and 7G). The dike is deformed by F_2 folds and is parallel to the composite S_1/S_2 foliation in the area. Zircons from this sample are euhedral, range between ~100 μm and ~350 μm in length, and have distinct core and rim domains. Eighteen individual LA-MC-ICP-MS analyses of 18 grain cores yielded $^{206}Pb/^{238}U$ dates that range from ca. 200 Ma to ca. 1.5 Ga, with an apparent cluster at 320.1 ± 6.7 Ma (MSWD = 0.9). U/Th values of core domains are generally <2, supporting an igneous origin. Twenty-six analyses of 26 grain rims yielded a weighted-mean $^{206}Pb/^{238}U$ age of 113.7 ± 2.3 Ma (MSWD = 0.6) (Fig. 9D).

Sample 15AB28 is an unfoliated tonalite pluton that crops out north of Adams Burn (Fig. 3). The host rock of the pluton displays a well-developed gneissic foliation. While this foliation is not currently correlated with the SABT described above, based on proximity to mapped SABT exposures, the pluton likely intruded after movement along the SABT (D_2). Zircon grains from 15AB28 are euhedral and >200 μm in their longest dimension. Six SHRIMP-RG analyses of six individual grains yielded a weighted-mean $^{206}Pb/^{238}U$ age of 111.0 ± 1.5 (MSWD = 1.6). A seventh spot was rejected from inclusion in the age calculation because it did not overlap with the majority of other spots in Tera-Wasserburg space (dashed ellipse in Fig. 9E). Together, samples 0519A and 15AB28 can be used to bracket timing of the approximately arc-normal displacements along the SABT. Deformation could have occurred between 116.0 Ma and 109.5 Ma, accounting for error associated with both ages.

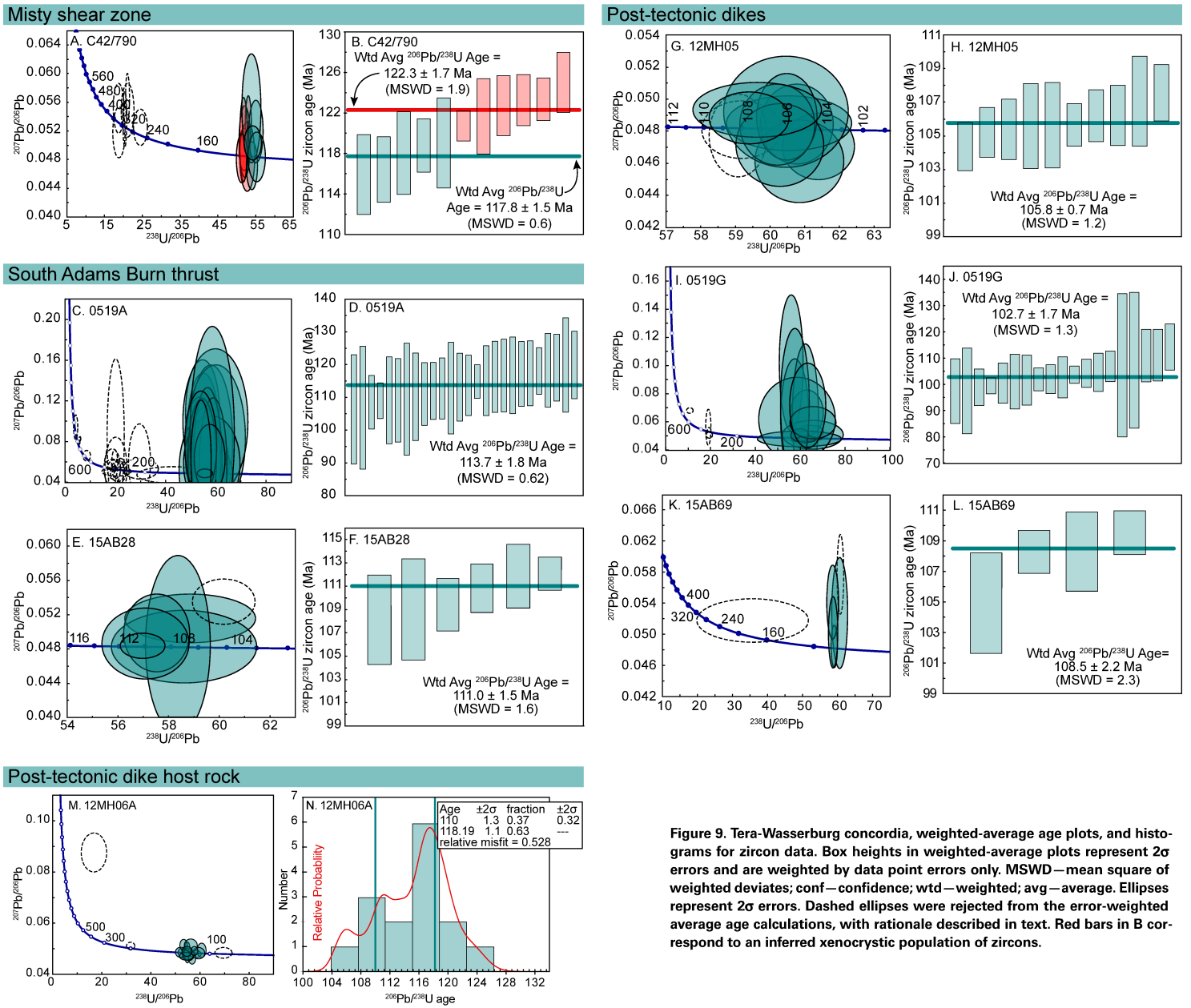

Figure 9. Tera-Wasserburg concordia, weighted-average age plots, and histograms for zircon data. Box heights in weighted-average plots represent 2σ errors and are weighted by data point errors only. MSWD—mean square of weighted deviates; conf—confidence; wtd—weighted; avg—average. Ellipses represent 2σ errors. Dashed ellipses were rejected from the error-weighted average age calculations, with rationale described in text. Red bars in B correspond to an inferred xenocrystic population of zircons.

Dike Arrays and Host Rock

Sample 12MH05 is a trondhjemitic post-tectonic dike collected from an outcrop of Irene Complex amphibolite gneiss south of point 1694 m (Fig. 3). Zircons from this sample are euhedral, display oscillatory zoning, and are typically >200 μm long. Ten SHRIMP-RG spots on ten individual zircon grains yielded a weighted-mean $^{206}Pb/^{238}U$ age of 105.8 ± 0.7 (MSWD = 1.2). An additional two analyses were excluded from the age calculation because they overlapped minimally with other spots in Tera-Wasserburg space (Fig. 9G).

Sample 0519G is a post-tectonic felsic dike collected from an outcrop of the Irene Complex south of point 1694 m (Fig. 3), from the same outcrop as sample 0519A (Fig. 7G). The dike crosscuts F_2 folds and is not visibly deformed. Zircons from this sample are euhedral, range between ~200 μm and ~60 μm in length, and have distinct core and rim domains. Four individual LA-MC-ICP-MS analyses were conducted on four zircon grains, yielding a weighted-mean $^{206}Pb/^{238}U$ age of 326.4 ± 8.8 Ma. Like sample 0519A, U/Th values for 0519G core spot analyses are low (<3, mean = 1.3), consistent with an igneous origin. Nineteen analyses of 0519G zircon rims (19 individual grains) yielded a weighted-mean $^{206}Pb/^{238}U$ age of 102.7 ± 2.0 Ma (2σ) (MSWD = 1.3).

Sample 15AB69 is a post-tectonic felsic dike collected from the footwall of a D_4-associated reverse fault north of Adams Burn (Fig. 3). The dike crosscuts an S_1/S_2 composite foliation, and both the dike and the foliation are deformed by folds that are localized to the area adjacent to the overlying reverse fault. These folds are SE-vergent, consistent with the top-to-the-SE displacement along the reverse fault, and unlike the top-to-the-NW sense of shear recorded in the SABT. Therefore, the deformation experienced by sample 15AB69 is likely associated with D_4, not D_2. Zircons from sample 15AB69 are euhedral, typically <200 μm long, and show oscillatory zoning. Four SHRIMP-RG analyses of four zircon grains yielded a weighted-mean $^{206}Pb/^{238}U$ age of 108.5 ± 2.2 (MSWD = 2.3). Two other analyses were rejected due to one being significantly older at 123.4 ± 0.7 Ma and the other being strongly discordant (Fig. 9K).

Sample 12MH06A is a deformed Irene Complex marble sample collected south of point 1694 m (Fig. 3). This marble hosts numerous, deformed felsic dikes. Zircon grains obtained from sample 12MH06A marble are subhedral and ~100–200 μm long. Grains have bright CL, oscillatory-zoned cores with darker rims. Sambridge and Compston (1994) mixture modeling analysis yielded two age populations at 118.2 ± 1.1 and 110.0 ± 1.3 Ma (Fig. 9M). The older age is consistent with ca. 119–117 Ma metamorphic zircon growth identified by Scott et al. (2009b) in pelitic schists ~30 km north of our field area. We interpret the younger date to be an additional age of metamorphism in the Irene Complex.

Geochronology results from the three dike samples described here suggest that crystallization occurred between 108.5 and 102.7 Ma, with a maximum range of 110.7–100.7 Ma, accounting for error. Crosscutting relationships between dikes and foliation indicate that the dike emplacement postdates D_2. The 110.0 Ma metamorphic zircon age in the Irene Complex marble suggests that conditions were suitable for zircon growth after D_2, at approximately the same time as emplacement of mid-crustal Separation Point Suite plutons.

Titanite Thermochronology and Trace-Element Thermometry

U-Pb Dates and Zr-in-Titanite Temperatures

Sample 12MH06 was collected from a calc-silicate exposure within the Irene Complex south of point 1694 m (Fig. 3). Titanite grains are typically anhedral and range in diameter from ~100 to ~300 μm. Eighteen grains were analyzed with 55 spots. Twelve of these grains were analyzed with a single spot. Of the remaining six grains analyzed with multiple spots, one grain was analyzed across much of its exposed surface with 24 spots. This ~300-μm-wide grain analyzed in detail has distinct rim, interior, and core domains, with the relatively high Th/U grain core yielding ^{207}Pb-corrected $^{206}Pb/^{238}U$ dates as old as 338 Ma (Fig. 10A). A series of spots surrounding the core (referred to as grain interior in Fig. 10) of the grain yield intermediate dates, and the youngest dates are preserved in the grain rim. For all 55 analysis spots, grain interiors yield a weighted-mean ^{207}Pb-corrected $^{206}Pb/^{238}U$ date of 111.7 ± 1.7 Ma (MSWD = 10.3), and the grain rims yield a weighted-mean ^{207}Pb-corrected $^{206}Pb/^{238}U$ date of 99.2 ± 1.6 Ma (MSWD = 3.1; Fig. 10D). The grain interior date from 12MH06 overlaps with the $^{206}Pb/^{238}U$ zircon age from 15AB28, a sample of the nearby post-D_2 tonalite described above. The rim domain of 12MH06 yields a date only slightly younger than inferred zircon crystallization ages of the post-tectonic dikes (12MH05, 0519G, and 15AB69). We evaluate the cause of these high MSWDs (Pb loss by volume diffusion or prolonged (re)crystallization) in the Discussion.

Zr-in-titanite temperatures calculated for sample 12MH06A range between 911 and 643 °C. Within the grain analyzed across its surface with 24 LASS-ICP-MS spots, 18 spots were analyzed for Zr concentration, and calculated temperatures range between 794 and 643 °C (Fig. 10C). Spots in the grain rim (spot dates <105 Ma) give an average temperature of 682 °C (1 SD = 12.8 °C), and spots in the interior and core domains give average temperatures of 762 °C (1 SD = 29.0 °C) and 704 °C (1 SD = 60.5 °C), respectively. Across all spot analyses in sample 12MH06A, there is a good negative correlation between temperature and date from ca. 138–120 Ma, which changes to a strong positive correlation between ca. 120 and 95 Ma (Figs. 10B and 11).

Evaluating Diffusive Loss of Pb and Zr in Titanite

Titanite is a useful mineral chronometer for studies of middle- and lower-crustal deformation due to its abundance in many metamorphic lithologies (Frost et al., 2000) and its ability to (re)crystallize during deformation (e.g., Müller and Franz, 2004; Spencer et al., 2013) while incorporating trace and rare-earth elements (e.g., Prowatke and Klemme, 2005, 2006; Spencer et al., 2013; Garber et al., 2017). The temperature- and pressure-sensitive incorporation of Zr^{+4} into the Ti^{+4} lattice site of titanite is particularly useful as a geothermometer (Hayden et al., 2008) that may be coupled with U-Pb dates to yield temperature-time histories (e.g., Kohn and Corrie, 2011; Spencer et al., 2013). However, co-located LASS-ICP-MS dates and Zr-in-titanite temperatures can

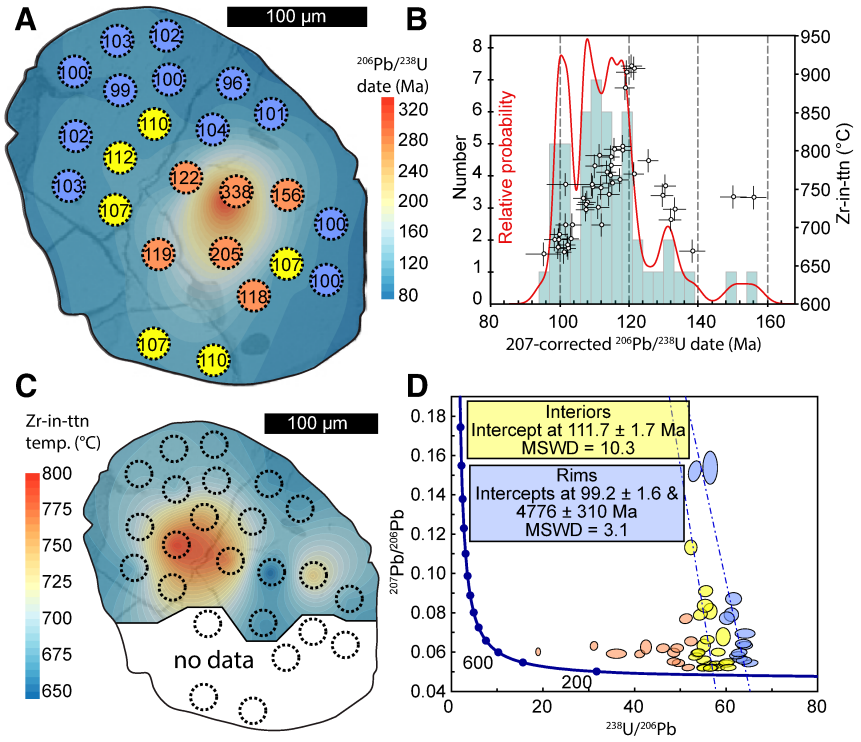

Figure 10. Sample 12MH06 U-Pb titanite thermochronology results. (A) Spot locations and ^{206}Pb/^{238}U dates of titanite grain with the greatest number of analyses. Spots are colored according to date and position within grain (orange—cores; yellow—interiors; blue—rims). Backscattered electron (BSE) image visible to show position of cracks relative to analysis spots. (B) Cumulative probability distribution and histogram plotted with calculated Zr-in-titanite temperatures (°C) for all analyses in sample 12MH06. Error bars represent 2σ uncertainty for ^{238}U/^{206}Pb dates and ±15 °C for temperatures. Histogram bin width is 3 m.y., starting at 85 Ma. (C) Same grain as A, contoured according to calculated Zr-in-titanite temperature. (D) Tera-Wasserburg concordia diagram including all 55 spots from 18 titanite grains. Ellipses are colored as in A. MSWD—mean square of weighted deviates. Contoured maps were generated using Surfer 11.0 software (http://www.goldensoftware.com/products/surfer).

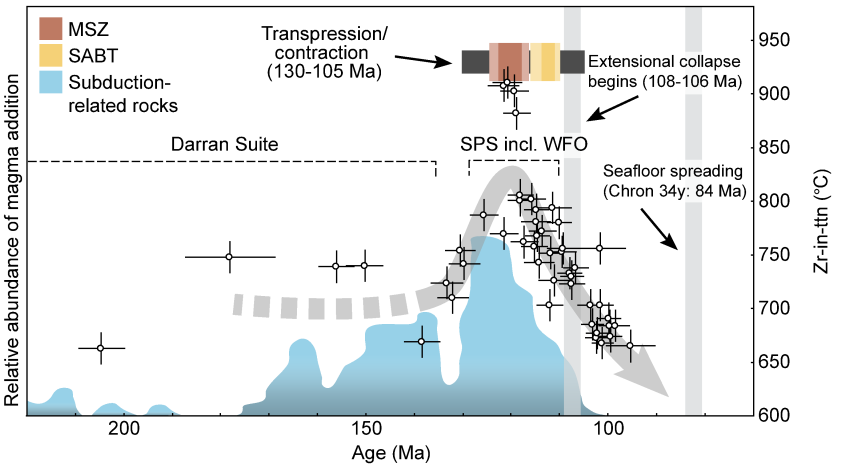

Figure 11. Zr-in-titanite temperature versus ^{206}Pb/^{238}U date. Error bars correspond to 2σ errors for date calculations and to ±15 °C for temperatures. Peak temperatures recorded in titanite from sample 12MH06 correspond with emplacement of the Western Fiordland Orthogneiss, followed by cooling at 5.9 ± 2.0 °C Ma^{-1} (least squares regression, 95% confidence interval (c.i.), assuming linear cooling and ignoring temperatures ≥882 °C) until ca. 95 Ma. Fiordland-wide magma abundance data after Mortimer and Campbell (2014). Regional structure and/or tectonic data from Schwartz et al. (2017). MSZ—Misty shear zone; SABT—South Adams Burn thrust.

only be considered together if it can be shown that no significant diffusive modification of titanite chemistry has occurred.

To investigate the extent of thermally mediated volume diffusion of Pb and Zr, we considered the characteristic diffusion lengths of the two cations given a peak temperature of 850 °C, which falls within the range of peak Cretaceous temperature for central Fiordland (800–920 °C, from Klepeis et al., 2007; De Paoli et al., 2009; Stowell et al., 2014; Schwartz et al., 2016). Length scales were calculated over a duration of 25 m.y., which reflects the duration of apparent cooling between peak Zr-in-titanite temperatures at ca. 120 Ma and the youngest U-Pb titanite date of ca. 95 Ma. Using the experimentally determined diffusivities of Zr (Cherniak, 2006) and Pb (Cherniak, 1993), we see that Pb and Zr are expected to diffuse over 660 μm and 70 μm, respectively. These lengths would result in modification of both Zr and Pb concentrations in much or all of our ~250-μm-wide grains. Even for a 1 m.y. duration of peak temperatures, Pb concentration would be influenced at the center of a 250-μm-wide grain. Instead, we see somewhat higher Pb concentration associated with younger dates (<125 Ma), and no trend of increasing Th/Pb with decreasing date (Fig. 12A), as would be expected if comparatively mobile Pb had diffused out of titanite. However, it is possible that some of that trend is masked by the proportion of non-radiogenic Pb included in total Pb. Additionally, we see a pattern of lower Zr concentration to higher Zr concentration back to lower Zr concentration from core to rim in titanite grains. This is inconsistent with diffusive modification of Zr in the analyzed titanite grains.

Furthermore, high field strength elements (HFSEs) and all rare-earth elements (REEs) in sample 12MH06 show a strong trend when plotted against ^{207}Pb-corrected $^{206}Pb/^{238}U$ date: HFSEs (specifically, Zr, Hf, and W) show a steady increase from ca. 150 Ma to ca. 120 Ma, and then a steady decrease from ca. 120 Ma to the youngest dates at ca. 95 Ma (Fig. 12B). All REEs show an opposing pattern, decreasing until ca. 120–115 Ma, and then increasing through ca. 95 Ma (Fig. 12C). Of particular interest is the anticorrelation of REE and Al concentrations, suggesting that Al is not involved with the substitution of REEs into the lattice of Adams Burn titanite, as has been shown experimentally by Prowatke and Klemme (2006), and observed elsewhere (Garber et al., 2017). The petrochronological significance of these trends in titanite is not discussed here, but they do support our assertion that there has been no significant diffusive modification of Zr or Pb concentrations (despite high calculated MSWDs), and that a temperature-time (T-t) history can be extracted from sample 12MH06, similar to the work of Schwartz et al. (2016).

DISCUSSION

Misty Shear Zone and South Adams Burn Thrust

In this contribution, we highlight two newly identified Early Cretaceous ductile structures that formed during emplacement of the WFO into a crustal-scale Carboniferous boundary. Here we discuss the following topics: (1) geochronological limits on the timing of activity of the two structures; (2) the timing of deformation relative to magmatism; (3) the geometry and kinematics of deformation; and (4) the vertical position of structures within the arc at the time of their formation. We use these four categories to track the migration of deformation through the lower and middle crust and to evaluate spatial and temporal changes in shear zone evolution within the Cretaceous arc.

Geochronology results indicate that the MSZ and SABT were active during a period of Fiordland-wide sinistral transpressional deformation that coincided with, and outlasted, WFO emplacement (e.g., Klepeis et al., 2004; Marcotte

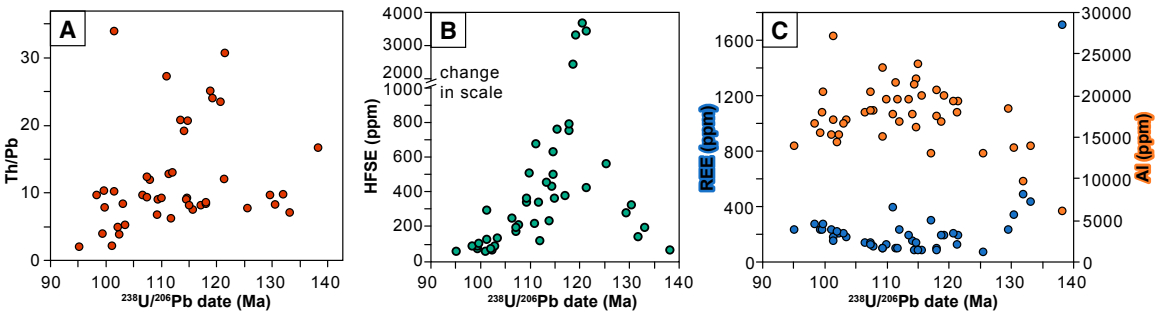

Figure 12. Evaluating diffusional modification of titanite chemistry. A-C include spot analyses that yielded U-Pb $^{206}Pb/^{238}U$ dates <140 Ma. (A) Th/Pb. Plot shows no trend of increasing Th/Pb with decreasing date, which would be expected if young dates were the result of diffusive Pb loss. (B) Plot of total of three tetravalent high field strength elements (HFSEs) (W, Zr, and Hf) (ppm). These HFSEs show a trend of increasing concentration from 140 to ca. 120 Ma, and then decreasing concentration from ca. 120–95 Ma. Other HFSEs (Nb and Ta) and P do not show this pattern. (C) Total rare-earth elements (REEs) (ppm) and Al (ppm). Aluminum and REEs show opposite trends, with REEs reaching a minimum and Al reaching a maximum between 120 and 110 Ma.

et al., 2005; Scott et al., 2011; Schwartz et al., 2016; Buriticá et al., 2019). Results from $^{206}Pb/^{238}U$ zircon geochronology indicate that the MSZ was active ca. 122.6–117.8 Ma, and the SABT was active sometime between ca. 113.7 and 111.0 Ma. The MSZ is slightly older than the SABT, and this suggests that MSZ and SABT architecture, kinematics, and position within the arc may represent changes in deformation style through time within the Early Cretaceous arc.

The MSZ and SABT partially coincide with the short-lived, 118–115 Ma emplacement of most of Fiordland's mafic to intermediate plutons (Schwartz et al., 2017). This is particularly evident for the ca. 123–118 Ma MSZ, which is defined by magmatic fabrics in the Misty Pluton. The preservation of these igneous structures within <300 m of the pluton margin suggests that, at least locally, the MSZ was abandoned prior to final crystallization of the pluton and that strain was localized elsewhere during much of the 118–115 Ma magmatic event. Similarly, deformation within the 114–111 Ma SABT coincided with emplacement of Separation Point Suite plutons across Fiordland between 129 and 110 Ma (Buriticá et al., 2019) and suites of felsic dikes in the field area. These observations indicate that deformation was spatially and temporally associated with magmatism, and that the MSZ in particular provides a rarely preserved record of transpressional deformation during flare-up magmatism.

The MSZ is defined by an S_2 foliation that dips gently to moderately to the north (average: 257, 25 N), and L_2 mineral lineations that plunge gently to the northeast. Kinematic indicators suggest top-to-the-southwest oblique-sinistral thrust motion. The trend of the average lineation orientation (20 > 040) is aligned to within 20° of the trend of the paleoarc axis (020, the elongation direction of plutons mapped by Turnbull et al., 2010), indicating that displacement was nearly parallel to the axis of the arc. By comparison, the SABT is defined by a subhorizontal, gently southeast-dipping S_2 (average: 035, 10 SE) containing a SE-trending L_2 (average: 18 > 140 for all measurements, 04 > 140 for measurements not influenced by late faulting) and is associated with NW-vergent folds (average axial surface: 012 17 SE). This NW-SE shortening direction is within 30° clockwise of the normal to the axis of the Cretaceous arc. This orientation is consistent with the larger system of sinistral transpression documented in Fiordland. Characteristics of the MSZ and SABT described here point to a change in the style of deformation within the field area: the ca. 123–118 Ma MSZ records primarily arc-parallel displacements, and the ca. 114–111 Ma SABT records mainly arc-normal shortening.

The MSZ formed along the margin of the Misty Pluton, which as part of the WFO, was emplaced at pressures estimated between 1.0 and 1.8 GPa (Bradshaw, 1989; Clarke et al., 2000; Allibone et al., 2009b; Allibone et al., 2009c; Daczko et al., 2009; De Paoli et al., 2009). The Misty Pluton was emplaced at pressures closer to ~1.1 GPa, according to the correlations and regional compilation of Klepeis et al. (2019a), which uses assemblages associated with peak metamorphic conditions during Cretaceous magmatism. The emplacement pressure of 1.1 GPa corresponds to a depth of ~41 km, assuming 0.1 GPa = 3.7 km. By comparison, the SABT formed within the Irene Complex, whose correlatives in central Fiordland record Cretaceous pressures estimated between ~0.42 and 0.88 GPa (Scott and Cooper, 2006; Scott et al., 2009a; Scott et al., 2009b). Using the same pressure-depth relationship, these pressures correspond to depths up to ~33 km. Although the Misty Pluton and the Irene Complex are currently juxtaposed at the surface, differences in recorded pressure indicate that the MSZ and SABT were active at different levels within the arc crustal column.

Based on the combined structural, geochronological, and geobarometric data summarized here, we favor a model of deformation in which the style of transpressional deformation and its location within the arc changed through time: during early emplacement of the WFO, deformation was localized along the margin of the Misty Pluton as a gently dipping shear zone recording mostly arc-parallel transport. Later, after WFO emplacement and crystallization, arc-normal displacements occurred in the middle crust along the SABT, a domain of subsolidus folding and shearing (Fig. 13). Between ca. 118 and 114 Ma, deformation in the Fiordland arc migrated vertically, and became increasingly partitioned in the middle crust.

Partitioned Transpression and Connections to Other Cretaceous Shear Zones and Ductile Thrusts in Fiordland

Misty Shear Zone

The ca. 123–118 Ma MSZ shows similarities to two other syn-magmatic shear zones operating in the Fiordland arc: the Mount Daniel shear zone (MDSZ) and the Grebe shear zone (GSZ) (Fig. 2). The MDSZ is located along the base of the 124.0–121.8 Ma WFO Worsely pluton (Schwartz et al., 2017, and references therein) and preserves exposures of magmatic fabrics and numerous intrusive sheets showing differing degrees of strain (Klepeis et al., 2004). The MDSZ therefore was active during emplacement of the WFO. Additional work of Bhattacharya et al. (2018) indicates that the MDSZ was active after Worsely emplacement until ca. 117 Ma or later based on the U-Pb zircon age of a weakly deformed dike. The MDSZ is truncated along with other expanses of the WFO by the subvertical, mostly postmagmatic sinistral transpressive Indecision Creek shear zone (ICSZ) active between 119 and 111 Ma (Klepeis et al., 2004; Marcotte et al., 2005). Activity of the GSZ is bracketed between 129 and 116 Ma (Scott et al., 2011; Buriticá et al., 2019), with the 122.8–119.9 Ma Puteketeke pluton of the SPS (Scott and Palin, 2008; Ramezani and Tulloch, 2009; Buriticá et al., 2019) displaying syn-magmatic folding compatible with transpressional deformation during pluton emplacement (Buriticá et al., 2019). These three early shear zones suggest that WFO and early SPS pluton margins were effective at localizing deformation. Stretching lineations in all three of the structures approach parallelism with the paleoarc axis and plunge gently or moderately (Klepeis et al., 2004; Scott et al., 2011), indicating a component of arc-parallel transport.

The MSZ is spatially associated with the George Sound shear zone (GSSZ), a >10-km-wide, steeply dipping, northeast-southwest–striking, subsolidus sinistral transpressional shear zone located north of the MSZ (Klepeis et al., 2004; Marcotte et al., 2005). Deformation in the GSSZ was active during the emplacement of a dioritic dike dated at 121.7 ± 4.2 Ma (U-Pb zircon, Marcotte

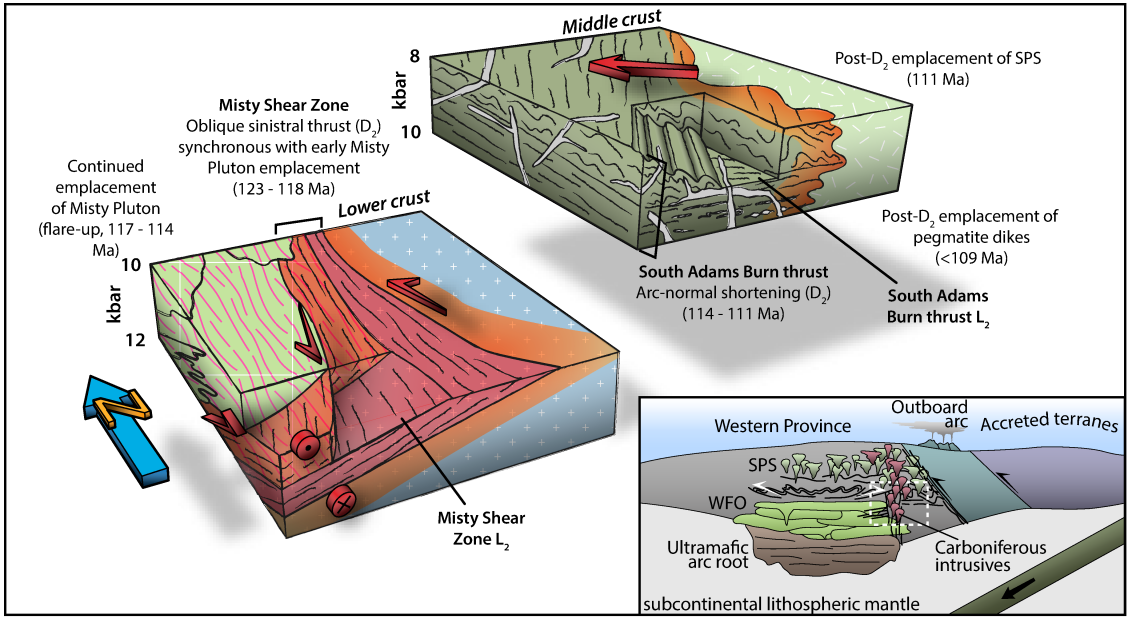

Figure 13. Cartoon reconstruction of area surrounding Cozette Burn prior to movement along Tertiary faults. Inset shows approximate location of Misty shear zone (MSZ) and South Adams Burn thrust (SABT) within a cross section of the arc. Rock units colored according to legend presented in Figures 2 and 3.

et al., 2005), and was likely active during the 119–111 Ma interval based on geometric and kinematic similarities with the Indecision Creek shear zone (Marcotte et al., 2005). The GSSZ extends from Bligh Sound in the north to where it was originally defined at George Sound (Klepeis et al., 2004). Turnbull et al. (2010) extended foliation trajectories associated with the GSSZ farther south to Coronation saddle (Figs. 2 and 3). We suggest here that the subsolidus fabrics mapped in the northern extent of our field area, while more scattered than the fabrics mapped by Klepeis et al. (2004), are correlative with the GSSZ based on their location, geometry, and shared subsolidus deformation textures. The nonuniform GSSZ fabrics presented in this study (Fig. 6C) are likely the result of the pervasive Cenozoic deformation documented by Klepeis et al. (2019b). The MSZ at its Camp 2 type locality is therefore a valuable record of ephemeral suprasolidus deformation prior to pluton crystallization and overprinting by a major subsolidus shear zone. Based on these associations, we interpret the MSZ to be the earliest documented expression of the GSSZ.

South Adams Burn Thrust

The arc-normal displacement of the SABT between ca. 114 and 111 Ma appears most similar to the 117–113 Ma (Schwartz et al., 2016) Caswell Sound fold and thrust belt (Fig. 2). Both localities record shortening at high angles to the Cretaceous arc over similar time intervals. Deformation at Caswell Sound is recognized as a bivergent north-south–striking fold and thrust belt along the upper contact of the WFO; this belt deforms both the WFO and its host rock (Daczko et al., 2002). Even though the SABT is not in contact with the WFO, it is similarly structurally higher than the Misty Pluton. We interpret the SABT and Caswell Sound fold and thrust belt to be correlative based on similarities in timing, structural level, and approximately arc-normal shortening directions. The extent of Early Cretaceous arc-normal shortening in Fiordland is therefore more widespread than previously recognized.

Coeval with the SABT and Caswell Sound fold and thrust belt are the ICSZ and GSSZ, two subvertical, primarily subsolidus, sinistral transpressive shear zones (Klepeis et al., 2004; Marcotte et al., 2005). In both the GSSZ and ICSZ, steeply dipping foliations contain steep stretching lineations that are characteristic of homogeneous transpressive deformation in which both simple shear and pure shear components are expressed in the same structure (Sanderson and Marchini, 1984; Fossen and Tikoff, 1993; Tikoff and Teyssier, 1994; Fossen and Tikoff, 1998). Nevertheless, these shear zones also show pronounced heterogeneity marked by discrete domains of dip-slip and oblique-slip displacements and fabrics relating to coaxial deformation, suggesting that at least locally, some partitioning of strain still occurred. Recent U-Pb titanite thermochronology of Buriticá et al. (2019) suggests that the MDSZ also continued to be active between at 111 Ma and as late as 106 Ma. Together, these relationships show clear evidence for kinematically partitioned transpression after emplacement of the WFO across Fiordland. Coeval accommodation of

arc-normal shortening in the Caswell fold and thrust belt and the SABT and sinistral transpression in the GSSZ and ICSZ and arc-oblique displacement in the MDSZ indicate that a component of shortening was partitioned outside of the subvertical shear zones and into the gently dipping layered packages of primarily metasedimentary gneisses. This suite of structures fits a partitioned style of transpression with a footprint extending beyond the margins of crystallized WFO plutons into the middle crust.

Timeline of Deformation, Magmatism, and Evolving Mid-Crustal Thermal Structure in Central Fiordland

Structural observations, zircon and titanite U-Pb geochronology, and Zr-in-titanite thermometry allow for detailed description of the dynamic magmatic, thermal, and deformation environment in the middle and lower crust of the Early Cretaceous arc, and also pick up details of earlier Carboniferous activity along an inherited boundary in central Fiordland. The ca. 338 Ma Carboniferous analysis from our U-Pb titanite thermochronology is consistent with regional metamorphism and emplacement of a linear belt of Carboniferous plutons (Allibone et al., 2009a, and references therein; Ramezani and Tulloch, 2009; Turnbull et al., 2010; Schwartz et al., 2016), suggesting that titanite in sample 12MH06 was (re)crystallizing long before the mantle-sourced (Decker et al., 2017), Early Cretaceous flare-up event emplaced the WFO adjacent to this boundary in the lower crust (Decker et al., 2017; Schwartz et al., 2017).

U-Pb zircon geochronology reveals the ephemeral nature of Early Cretaceous deformation within and adjacent to this long-lived crustal boundary. At the margin of the Misty Pluton in the lower crust, MSZ activity between ca. 123 and 118 Ma (and potentially earlier) occurred as oblique sinistral-reverse shearing with largely arc-parallel displacements along a gently dipping plane parallel to the pluton contact. As early (pre ca. 118–115 Ma flare-up) pulses of Misty Pluton began to crystallize, the character of deformation in the lower crust changed significantly. The subsolidus, steeply dipping transpressional George Sound and Indecision Creek shear zones deform WFO plutons, including the Misty Pluton north of Adams Burn as early as ca. 122 Ma, but primarily through the interval of ca. 119–111 Ma (Marcotte et al., 2005; Buriticá et al., 2019). WFO (including the Misty Pluton) magmatism continued elsewhere in the lower crust, primarily between ca. 118 and 115 Ma (Schwartz et al., 2016, 2017), while at mid-crustal levels, arc-normal shortening along the SABT was accommodated in layered Paleozoic rocks. Shortening occurred between ca. 114 and 111 Ma, and was outlasted by magmatism in the form of a tonalitic pluton emplaced at ca. 111 Ma and numerous pegmatite dikes intruded between ca. 109 and 103 Ma.

Although the mid-crustal exposures have a slightly younger history of deformation and magmatism than the lower crust in the study area, titanite trace-element thermometry indicates that the thermal structure of the middle crust is very similar to that of the lower crust. Zr-in-titanite temperatures calculated for sample 12MH06 suggest that the host rock of the SABT reached peak temperatures (>800 °C) between ca. 120 and 118 Ma, prior to the mid-crustal deformation and magmatism recorded in the study area, and coincident with the onset of flare-up magmatism of much of the WFO. Sample 12MH06 yields a T-t path showing slow cooling at 5.9 ± 2.0 °C Ma^{-1} (least squares regression, 95% confidence interval) between ca. 118 and 95 Ma, indicating a middle crust that remained hot (>750 °C) for ~7 m.y., from ca. 118–111 Ma. Temperatures remained above 650 °C through 95 Ma, and we see no clear change in the T-t path at 108–106 Ma, at the onset of extensional collapse in Fiordland (Fig. 11) (Klepeis et al., 2007; Schwartz et al., 2016). Our titanite thermometry results are consistent with the ca. 111 Ma crystallization age of a nearby SPS tonalitic pluton, ca. 110 Ma metamorphic zircon growth in the Irene Complex, and with ongoing, post-tectonic leucocratic dike emplacement in central Fiordland between ca. 109 and 103 Ma (reported here), and elsewhere in Fiordland as young as 97 Ma (Klepeis et al., 2007). Schwartz et al. (2016) suggest this extended period of dike emplacement is associated with a thermal pulse that caused particularly slow cooling at 8.3 ± 6.6 °C Ma^{-1} in their titanite samples from lower-crustal exposures of the WFO.

The thermal state of the middle and lower crust and the record of WFO crystallization may explain the vertical migration and change in style of deformation during and after the Early Cretaceous magma flare-up event. The MSZ accommodated oblique sinistral-reverse offset during early emplacement of the Misty Pluton between ca. 123 and 118 Ma and was abandoned at the onset of the emplacement of much of the WFO between 118 and 115 Ma (Schwartz et al., 2017). At ca. 115 Ma, both the lower and middle crust were hot (>750 °C), based on the Zr-in-titanite results presented here and by Schwartz et al. (2016). Additionally, most of the lower-crustal WFO had been emplaced and crystallized, as evidenced by subsolidus fabrics deforming the WFO as part of the GSSZ and ICSZ between ca. 119 and 111 Ma (Marcotte et al., 2005; Buriticá et al., 2019). This time marks a fundamental shift in the behavior of the arc and the style of deformation: after crystallization of much of the WFO, and in the absence of any strong thermal gradients (both the lower and middle crust were hot), transpressional deformation became kinematically partitioned. Arc-normal shortening was accommodated within the layered packages of Paleozoic metasedimentary rocks, and an additional component of pure shear as well as simple shear was taken up in the steeply dipping ICSZ and GSSZ. This suggests that sustained elevated temperatures in the middle crust not only primed the Early Cretaceous arc for extensional orogenic collapse between 108 and 106 Ma, as presented by Schwartz et al. (2016), but also strongly influenced the expression of the last phase of transpressional deformation during and after WFO crystallization. These elevated temperatures facilitated a vertical migration of deformation within the arc and a transition from apparently homogeneous deformation to kinematically partitioned transpression.

Role of the Reactivated Paleozoic Fabrics and Crustal Boundary

The timing of pluton crystallization in the lower crust accompanied by elevated middle- and lower-crustal temperatures provides a viable mechanism

by which deformation migrated vertically through the Early Cretaceous arc. The location and geometry of the MSZ and SABT, however, can be better understood by also considering structural reactivation of the Carboniferous boundary inferred by Andico et al. (2017) and Klepeis et al. (2019a) and of inherited fabrics in Paleozoic gneisses and schists. We see potential influence of structural inheritance in both the SABT and MSZ. In the SABT, the gently dipping high-strain zone and domain of NW-vergent folds are concentrated in a layered package of Paleozoic gneisses and schists. The Paleozoic fabric, typically defined by biotite and hornblende, is well suited for reactivation compared to, for example, more isotropic volumes of the WFO. In the absence of large temperature differences between the middle and lower crust, it is likely that favorably oriented mineralogical weakness in mid-crustal metasedimentary rocks promoted the localization of arc-normal shortening.

For the MSZ, its gently to moderately dipping geometry differs from early models of transpression in which a steeply dipping zone accommodates pure and simple shear to produce horizontal shortening and vertical extrusion (Sanderson and Marchini, 1984). Although modified to include non-vertical boundaries (inclined transpression; Jones et al., 2004), and melt-facilitated kinematic partitioning (e.g., Tikoff and Saint Blanquat, 1997; Saint Blanquat et al., 1998), models of transpression have not explicitly considered pluton geometry as a factor influencing shear zone orientation. The MSZ is localized along the contact of the Misty Pluton, consistent with magmatism acting to focus deformation at sites of high rheologic contrast. The MSZ, however, differs from models of kinematic partitioning in which plutons tend to facilitate steeply dipping strike-slip shear zones. Instead, MSZ geometry is compatible with that of many lower-crustal intrusions, which tend to be emplaced as subhorizontal tabular bodies (e.g., Saleeby et al., 2003; Economos et al., 2009; Miller et al., 2009; Needy et al., 2009). It is possible therefore that pluton geometry exerts significant control on shear-zone orientation in the lower crust.

The SABT and MSZ both occur within the inferred Paleozoic crustal boundary based on the ~5-km-wide linear belt of Carboniferous plutons and sharp $\delta^{18}O$ gradients of Jurassic intrusives (Andico et al., 2017; Klepeis et al., 2019a). This boundary is exposed within lower- and middle-crustal blocks with no offset or significant changes in trend along its length approximately parallel to the trend of the arc, indicating that it is steeply dipping. The orientation of the boundary therefore likely did not control the geometry of the gently dipping SABT or MSZ; however, it probably significantly influenced the location of the structures within the arc. The Paleozoic boundary discussed in this contribution also coincides with the George Sound shear zone (Klepeis et al., 2004), and a second crustal-scale structure to the east coincides with the Indecision Creek and Grebe shear zones (Scott et al., 2011; Buriticá et al., 2019; Klepeis et al., 2019a). To that end, the inherited boundary acted to localize significant amounts of deformation, and the preexisting anisotropies within the ~5-km-wide zone were reactivated during widespread Cretaceous transpression.

Additionally, the inherited Paleozoic boundary helps to explain why the middle and lower crust reached similar elevated temperatures in the Early Cretaceous. Preexisting structures are recognized as important conduits for the transport of melt and fluids (e.g., Kerrich and Feng, 1992; Román-Berdiel et al., 1997; Brown et al., 2011), and we see evidence of this in Fiordland. In eastern Fiordland, Allibone et al. (2010) document Cretaceous hydrothermal mineralization associated with a segment of the Grebe shear zone along the suture of an outboard arc with the Carboniferous Gondwana margin. Primarily in western Fiordland, in the lower crustal block described by Klepeis et al. (2019a), Schwartz et al. (2016) found evidence for a thermal pulse associated with amphibolite-facies conditions and widespread emplacement of A-type granitic dikes. We found a similar record of elevated Zr-in-titanite temperatures and accompanying granitic dike emplacement in the mid-crustal exposures of central Fiordland, and suggest that the inferred Carboniferous boundary may have acted as an efficient conduit for transporting melt vertically. Thermal modeling (e.g., Depine et al., 2008) indicates that melt migration can produce uniform, elevated temperatures in the middle and lower crust, which in turn influences the expression of deformation. This expression provides an explanation for SABT initiation in thermally weakened rocks of the middle crust and enhances our understanding of the relationship between deformation and magmatism in Fiordland. Marcotte et al. (2005) found evidence for only small volumes of melt conveyed through the primarily subsolidus Indecision Creek shear zone, and recognized examples of suprasolidus shearing in the MSZ (this study), the Mount Daniel shear zone (Klepeis et al., 2004), and portions of the Grebe shear zone (Scott et al., 2011; Buriticá et al., 2019) all involve gently to moderately dipping foliations. These observations suggest that transpressional deformation in Fiordland may not have been the only mechanism by which melt was transported upward from the lower crust to form mid-crustal plutons. Deformation and magmatism show a spatio-temporal association, but it is likely that the crustal-scale boundaries, along which magmatism and transpressional deformation localized, acted as conduits for transmitting melt from lower- to mid-crustal levels.

CONCLUSIONS

Our study highlights two newly described structures in central Fiordland that were active during Early Cretaceous arc magmatism along the Gondwana margin: The Misty shear zone (MSZ) and the South Adams Burn thrust (SABT). The MSZ records dominantly arc-parallel motion along a gently dipping shear zone between at least ca. 123 and 118 Ma, localized along the margin of the lower-crustal WFO during its early emplacement. The MSZ is interpreted to be an early strand of the mostly postmagmatic George Sound shear zone. The SABT accommodated arc-normal shortening between ca. 114 and 111 Ma at mid-crustal levels in a layered package of Paleozoic rocks. Both the MSZ and SABT are located within an inferred Paleozoic crustal boundary. Deformation within the boundary migrated from the lower to middle crust between ca. 118 and 114 Ma, when most of the WFO was emplaced and crystallized in the lower crust. During this time, the architecture and kinematics of deformation changed substantially and show evidence for influence by inherited structures. The gently dipping MSZ does not fit models for the arc-parallel component

of transpression commonly localized along magmatic arcs (e.g., Tikoff and Saint Blanquat, 1997; Blanquat et al., 1998) and likely reflects the tabular geometry of the Misty Pluton. Arc-normal deformation of the SABT reactivates gneissic layering in Paleozoic rock units, contributing to the kinematically partitioned style of deformation that expanded across much of the mid-crust (Daczko et al., 2002; Klepeis et al., 2004; Marcotte et al., 2005; Schwartz et al., 2016; Schwartz et al., 2017; Buriticá et al., 2019).

The pronounced shift in the accommodation of deformation within the arc between 118 and 114 Ma is attributable to the thermal structure of the middle and lower crust. U-Pb titanite geochronology and trace-element thermometry analyses from a mid-crustal calc-silicate exposure indicate that titanite from a single outcrop records a protracted history of (re)crystallization along an inferred Paleozoic crustal-scale boundary from ca. 338 Ma to 95 Ma. Zr-in-titanite temperatures show that the mid-crust reached peak temperatures (>800 °C) at the onset of lower-crustal flare-up magmatism (ca. 118 Ma) and remained hot (>750 °C) until 111 Ma. The T-t path calculated indicates slow cooling at 5.9 ± 2.0 °C Ma^{-1} through 95 Ma, consistent with metamorphic Zr-in-titanite temperatures calculated by Schwartz et al. (2016) for the lower crust over a similar time interval. Both the middle and lower crust experienced sustained elevated temperatures, and without any large thermal gradient between the two levels following WFO crystallization, transpression became kinematically partitioned. Arc-normal shortening was concentrated in rheologically weak layered Paleozoic rocks such as in the SABT between ca. 114 and 111 Ma. The old boundary likely served as a conduit for vertical transport of melt during the Early Cretaceous, which may in turn have facilitated uniformly elevated temperatures in the middle and lower crust and subsequent vertical migration of deformation. Results show that both magmatism and deformation tend to concentrate in inherited, crustal-scale structures, and that the spatio-temporal patterns of deformation in the middle and lower crust are sensitive to the thermal structure of the boundary and to magma crystallization in the lower crust.

ACKNOWLEDGMENTS

We gratefully acknowledge the Department of Land Conservation for permission to sample, and GNS Science for facilitating field work and initial sample processing. We thank Dr. Andy Tulloch for discussions and assistance and John Gilbert for help with field data collection and interpretation. Two $^{206}Pb/^{238}U$ zircon dates used in this study (from samples 0519A and 0519G) were acquired at the Arizona LaserChron Center at the University of Arizona. We thank the Arizona LaserChron Center and Dr. George Gehrels for their essential roles in this portion of our geochronological analyses. This manuscript benefited from constructive comments by Dr. Robert Miller and an anonymous reviewer. Financial support for this work was provided by National Science Foundation grants EAR-1119248 and EAR-1650183.

REFERENCES CITED

Allibone, A., Ashley, P., MacKenzie, D., and Craw, D., 2010, Shear-hosted base metal mineralisation at the Dana Peaks, Murchison Mountains, Fiordland, New Zealand: New Zealand Journal of Geology and Geophysics, v. 53, p. 271–294, https://doi.org/10.1080/00288306.2010.498406.

Allibone, A.H., Turnbull, I.M., Tulloch, A.J., and Cooper, A.F., 2007, Plutonic rocks of the Median Batholith in southwest Fiordland, New Zealand: Field relations, geochemistry, and correlation: New Zealand Journal of Geology and Geophysics, v. 50, p. 283–314, https://doi.org/10.1080/00288300709509838.

Allibone, A.H., Jongens, R., Scott, J.M., Tulloch, A.J., Turnbull, I.M., Cooper, A.F., Powell, N.G., Ladley, E.B., King, R.P., and Rattenbury, M.S., 2009a, Plutonic rocks of the Median Batholith in eastern and central Fiordland, New Zealand: Field relations, geochemistry, correlation, and nomenclature: New Zealand Journal of Geology and Geophysics, v. 52, p. 101–148, https://doi.org/10.1080/00288300909509882.

Allibone, A.H., Jongens, R., Turnbull, I.M., Milan, L.A., Daczko, N.R., DePaoli, M.C., and Tulloch, A.J., 2009b, Plutonic rocks of Western Fiordland, New Zealand: Field relations, geochemistry, correlation, and nomenclature: New Zealand Journal of Geology and Geophysics, v. 52, p. 379–415, https://doi.org/10.1080/00288306.2009.9518465.

Allibone, A.H., Milan, L.A., Daczko, N.R., and Turnbull, I.M., 2009c, Granulite facies thermal aureoles and metastable amphibolite facies assemblages adjacent to the Western Fiordland Orthogneiss in southwest Fiordland, New Zealand: Journal of Metamorphic Geology, v. 27, p. 349–369, https://doi.org/10.1111/j.1525-1314.2009.00822.x.

Andico, S., Schwartz, J.J., Tulloch, A., Turnbull, R., Klepeis, K., Miranda, E.A., Kitajima, K., and Ringwood, M.F., 2017, Oxygen isotope mapping reveals a crustal-scale structure within the Median Batholith, Fiordland, New Zealand: Geological Society of America Abstracts with Programs, v. 49, no. 6, https://doi.org/10.1130/abs/2017AM-305151.

Bhattacharya, S., Kemp, A.I.S., and Collins, W.J., 2018, Response of zircon to melting and metamorphism in deep arc crust, Fiordland (New Zealand): Implications for zircon inheritance in cordilleran granites: Contributions to Mineralogy and Petrology, v. 173, p. 28, https://doi.org/10.1007/s00410-018-1446-5.

Bitencourt, M.F., and Nardi, L.V.S., 2000, Tectonic setting and sources of magmatism related to the southern Brazilian Shear Belt: Revista Brasileira de Geociencias, v. 30, p. 186–189, https://doi.org/10.25249/0375-7536.2000301186189.

Bradshaw, J.Y., 1989, Origin and metamorphic history of an Early Cretaceous polybaric granulite terrain, Fiordland, southwest New Zealand: Contributions to Mineralogy and Petrology, v. 103, p. 346–360, https://doi.org/10.1007/BF00402921.

Brown, M., Korhonen, F.J., and Siddoway, C.S., 2011, Organizing melt flow through the crust: Elements, v. 7, p. 261–266, https://doi.org/10.2113/gselements.7.4.261.

Buriticá, L.F., Schwartz, J.J., Klepeis, K.A., Miranda, E.A., Tulloch, A.J., Coble, M.A., and Kylander-Clark, A.R.C., 2019, Temporal and spatial variations in magmatism and transpression in a Cretaceous arc, Median Batholith, Fiordland, New Zealand: Lithosphere, v. 11, p. 652–682, https://doi.org/10.1130/L1073.1.

Chan, C.F., Shea, E.K., Kent, A.J.R., Miller, R.B., Miller, J.S., and Bowring, S.A., 2017, Formation of a sheeted intrusive complex within the deep-crustal Tenpeak pluton, North Cascades, Washington: Geosphere, v. 13, p. 1610–1639, https://doi.org/10.1130/GES01323.1.

Chapman, A.D., Saleeby, J.B., Wood, D.J., Piasecki, A., Kidder, S., Ducea, M.N., and Farley, K.A., 2012, Late Cretaceous gravitational collapse of the southern Sierra Nevada batholith, California: Geosphere, v. 8, p. 314–341, https://doi.org/10.1130/GES00740.1.

Cherniak, D.J., 1993, Lead diffusion in titanite and preliminary results on the effects of radiation damage on Pb transport: Chemical Geology, v. 110, p. 177–194, https://doi.org/10.1016/0009-2541(93)90253-F.

Cherniak, D.J., 2006, Zr diffusion in titanite: Contributions to Mineralogy and Petrology, v. 152, p. 639–647, https://doi.org/10.1007/s00410-006-0133-0.

Clarke, G.L., Klepeis, K.A., and Daczko, N.R., 2000, Cretaceous high-P granulites at Milford Sound, New Zealand: Metamorphic history and emplacement in a convergent margin setting: Journal of Metamorphic Geology, v. 18, p. 359–374, https://doi.org/10.1046/j.1525-1314.2000.00259.x.

Condie, K.C., 2014, Growth of continental crust: A balance between preservation and recycling: Mineralogical Magazine, v. 78, p. 623–637, https://doi.org/10.1180/minmag.2014.078.3.11.

Condie, K.C., and Kröner, A., 2013, The building blocks of continental crust: Evidence for a major change in the tectonic setting of continental growth at the end of the Archean: Gondwana Research, v. 23, p. 394–402, https://doi.org/10.1016/j.gr.2011.09.011.

Daczko, N.R., Klepeis, K.A., and Clarke, G.L., 2001, Evidence of Early Cretaceous collisional-style orogenesis in northern Fiordland, New Zealand and its effects on the evolution of the lower crust: Journal of Structural Geology, v. 23, p. 693–713, https://doi.org/10.1016/S0191-8141(00)00130-9.

Daczko, N.R., Klepeis, K.A., and Clarke, G.L., 2002, Thermomechanical evolution of the crust during convergence and deep crustal pluton emplacement in the Western Province of Fiordland, New Zealand: Crustal evolution during convergence: Tectonics, v. 21, https://doi.org/10.1029/2001TC001282.

Daczko, N.R., Milan, L.A., and Halpin, J.A., 2009, Metastable persistence of pelitic metamorphic assemblages at the root of a Cretaceous magmatic arc—Fiordland, New Zealand: Journal of Metamorphic Geology, v. 27, p. 233–247, https://doi.org/10.1111/j.1525-1314.2009.00815.x.

De Paoli, M.C., Clarke, G.L., Klepeis, K.A., Allibone, H., and Turnbull, I.M., 2009, The Eclogite-Granulite Transition: Mafic and Intermediate Assemblages at Breaksea Sound, New Zealand: Journal of Petrology, v. 50, p. 2307–2343, https://doi.org/10.1093/petrology/egp078.

DeCelles, P.G., Zandt, G., Beck, S.L., Currie, C.A., Ducea, M.N., Kapp, P., Gehrels, G.E., Carrapa, B., Quade, J., and Schoenbohm, L.M., 2015, Cyclical orogenic processes in the Cenozoic central Andes, *in* DeCelles, P.G., Ducea, M.N., Carrapa, B., and Kapp, P.A., eds., Geodynamics of a Cordilleran Orogenic System: The Central Andes of Argentina and Northern Chile: Geological Society of America Memoir 212, p. 459–490, https://doi.org/10.1130/2015.1212(22).

Decker, M., Schwartz, J.J., Stowell, H.H., Klepeis, K.A., Tulloch, A.J., Kitajima, K., Valley, J.W., and Kylander-Clark, A.R.C., 2017, Slab-triggered arc flare-up in the Cretaceous Median Batholith and the growth of lower arc crust, Fiordland, New Zealand: Journal of Petrology, v. 58, p. 1145–1171, https://doi.org/10.1093/petrology/egx049.

Depine, G.V., Andronicos, C.L., and Phipps-Morgan, J., 2008, Near-isothermal conditions in the middle and lower crust induced by melt migration: Nature, v. 452, p. 80–83, https://doi.org/10.1038/nature06689.

Ducea, M., 2001, The California Arc: Thick granitic batholiths, eclogitic residues, lithospheric-scale thrusting, and magmatic flare-ups: GSA Today, v. 11, no. 11, p. 4–10, https://doi.org/10.1130/1052-5173(2001)011<0004:TCATGB>2.0.CO;2.

Ducea, M.N., and Barton, M.D., 2007, Igniting flare-up events in Cordilleran arcs: Geology, v. 35, no. 11, p. 1047–1050, https://doi.org/10.1130/G23898A.1.

Ducea, M.N., Paterson, S.R., and DeCelles, P.G., 2015a, High-volume magmatic events in subduction systems: Elements, v. 11, p. 99–104, https://doi.org/10.2113/gselements.11.2.99.

Ducea, M.N., Saleeby, J.B., and Bergantz, G., 2015b, The architecture, chemistry, and evolution of continental magmatic arcs: Annual Review of Earth and Planetary Sciences, v. 43, p. 299–331, https://doi.org/10.1146/annurev-earth-060614-105049.

Economos, R.C., Memeti, V., Paterson, S.R., Miller, J.S., Erdmann, S., and Žák, J., 2009, Causes of compositional diversity in a lobe of the Half Dome granodiorite, Tuolumne Batholith, Central Sierra Nevada, California: Earth and Environmental Science Transactions of the Royal Society of Edinburgh, v. 100, p. 173–183, https://doi.org/10.1017/S1755691009016065.

Economos, R.C., Paterson, S.R., Said, L.O., Ducea, M.N., Anderson, J.L., and Padilla, A.J., 2012, Gobi-Tianshan connections: Field observations and isotopes from an early Permian arc complex in southern Mongolia: Geological Society of America Bulletin, v. 124, p. 1688–1701, https://doi.org/10.1130/B30324.1.

Fitch, T.J., 1972, Plate convergence, transcurrent faults, and internal deformation adjacent to Southeast Asia and the western Pacific: Journal of Geophysical Research, v. 77, p. 4432–4460, https://doi.org/10.1029/JB077i023p04432.

Fossen, H., and Tikoff, B., 1993, The deformation matrix for simultaneous simple shearing, pure shearing and volume change, and its application to transpression-transtension tectonics: Journal of Structural Geology, v. 15, p. 413–422, https://doi.org/10.1016/0191-8141(93)90137-Y.

Fossen, H., and Tikoff, B., 1998, Extended models of transpression and transtension, and application to tectonic settings, *in* Holdsworth, R.E., Strachan, R.A., and Dewey, J.F., eds., Continental Transpressional and Transtensional Tectonics: Geological Society of London Special Publication 135, p. 15–33.

Frost, B.R., Chamberlain, K.R., and Schumacher, J.C., 2000, Sphene (titanite): Phase relations and role as a geochronometer: Chemical Geology, v. 172, p. 131–148, https://doi.org/10.1016/S0009-2541(00)00240-0.

Furlong, K.P., and Kamp, P.J.J., 2009, The lithospheric geodynamics of plate boundary transpression in New Zealand: Initiating and emplacing subduction along the Hikurangi margin, and the tectonic evolution of the Alpine Fault system: Tectonophysics, v. 474, p. 449–462, https://doi.org/10.1016/j.tecto.2009.04.023.

Garber, J.M., Hacker, B.R., Kylander-Clark, A.R.C., Stearns, M., and Seward, G., 2017, Controls on trace element uptake in metamorphic titanite: Implications for petrochronology: Journal of Petrology, v. 58, p. 1031–1057, https://doi.org/10.1093/petrology/egx046.

Hawkesworth, C., Cawood, P.A., and Dhuime, B., 2019, Rates of generation and growth of the continental crust: Geoscience Frontiers, v. 10, p. 165–173, https://doi.org/10.1016/j.gsf.2018.02.004.

Hayden, L.A., Watson, E.B., and Wark, D.A., 2008, A thermobarometer for sphene (titanite): Contributions to Mineralogy and Petrology, v. 155, p. 529–540, https://doi.org/10.1007/s00410-007-0256-y.

Holdsworth, R.E., Butler, C.A., and Roberts, A.M., 1997, The recognition of reactivation during continental deformation: Journal of the Geological Society of London, v. 154, p. 73–78, https://doi.org/10.1144/gsjgs.154.1.0073.

Ireland, T.R., and Gibson, G.M., 1998, SHRIMP monazite and zircon geochronology of high-grade metamorphism in New Zealand: Journal of Metamorphic Geology, v. 16, p. 149–167, https://doi.org/10.1111/j.1525-1314.1998.00112.x.

Jones, R.R., Holdsworth, R.E., Clegg, P., McCaffrey, K., and Tavarnelli, E., 2004, Inclined transpression: Journal of Structural Geology, v. 26, p. 1531–1548, https://doi.org/10.1016/j.jsg.2004.01.004.

Kerrich, R., and Feng, R., 1992, Archean geodynamics and the Abitibi-Pontiac collision: Implications for advection of fluids at transpressive collisional boundaries and the origin of giant quartz vein systems: Earth-Science Reviews, v. 32, p. 33–60, https://doi.org/10.1016/0012-8252(92)90011-H.

Kimbrough, D.L., Tulloch, A.J., Coombs, D.S., Landis, C.A., Johnston, M.R., and Mattinson, J.M., 1994, Uranium-lead zircon ages from the Median Tectonic Zone, New Zealand: New Zealand Journal of Geology and Geophysics, v. 37, p. 393–419, https://doi.org/10.1080/00288306.1994.9514630.

King, P.R., 2000, Tectonic reconstructions of New Zealand: 40 Ma to the Present: New Zealand Journal of Geology and Geophysics, v. 43, p. 611–638, https://doi.org/10.1080/00288306.2000.9514913.

Klepeis, K.A., Clarke, G.L., and Rushmer, T., 2003, Magma transport and coupling between deformation and magmatism in the continental lithosphere: GSA Today, v. 13, no. 1, p. 4–11, https://doi.org/10.1130/1052-5173(2003)013<0004:MTACBD>2.0.CO;2.

Klepeis, K.A., Clarke, G.L., Gehrels, G., and Vervoort, J., 2004, Processes controlling vertical coupling and decoupling between the upper and lower crust of orogens: Results from Fiordland, New Zealand: Journal of Structural Geology, v. 26, p. 765–791, https://doi.org/10.1016/j.jsg.2003.08.012.

Klepeis, K.A., King, D., De Paoli, M., Clarke, G.L., and Gehrels, G., 2007, Interaction of strong lower and weak middle crust during lithospheric extension in western New Zealand: Continental extension in New Zealand: Tectonics, v. 26, https://doi.org/10.1029/2006TC002003.

Klepeis, K.A., Schwartz, J., Stowell, H., and Tulloch, A., 2016, Gneiss domes, vertical and horizontal mass transfer, and the initiation of extension in the hot lower-crustal root of a continental arc, Fiordland, New Zealand: Lithosphere, v. 8, p. 116–140, https://doi.org/10.1130/L490.1.

Klepeis, K., Webb, L., Blatchford, H., Schwartz, J., Jongens, R., Turnbull, R., and Stowell, H., 2019a, Deep slab collision during Miocene subduction causes uplift along crustal-scale reverse faults in Fiordland, New Zealand: GSA Today, https://doi.org/10.1130/GSATG399A.1.

Klepeis, K.A., Webb, L.E., Blatchford, H.J., Jongens, R., Turnbull, R., and Schwartz, J.J., 2019b, The age and origin of Miocene–Pliocene fault reactivations in the upper plate of an incipient subduction zone, Puysegur Margin, New Zealand: Tectonics, v. 38, no. 8, p. 3237–3260, https://doi.org/10.1029/2019TC005674.

Kohn, M.J., and Corrie, S.L., 2011, Preserved Zr-temperatures and U-Pb ages in high-grade metamorphic titanite: Evidence for a static hot channel in the Himalayan orogen: Earth and Planetary Science Letters, v. 311, p. 136–143, https://doi.org/10.1016/j.epsl.2011.09.008.

Lebrun, J.-F., Lamarche, G., and Collot, J.-Y., 2003, Subduction initiation at a strike-slip plate boundary: The Cenozoic Pacific-Australian plate boundary, south of New Zealand: Subduction initiation at strike-slip boundary: Journal of Geophysical Research. Solid Earth, v. 108, no. B9, https://doi.org/10.1029/2002JB002041.

Lehmann, J., Schulmann, K., Lexa, O., Závada, P., Štípská, P., Hasalová, P., Belyanin, G., and Corsini, M., 2017, Detachment folding of partially molten crust in accretionary orogens: A new magma-enhanced vertical mass and heat transfer mechanism: Lithosphere, v. 9, p. 889–909, https://doi.org/10.1130/L670.1.

Lu, Y., Kerrich, R., Cawood, P.A., McCuaig, T.C., Hart, C.J.R., Li, Z., Hou, Z., and Bagas, L., 2012, Zircon SHRIMP U-Pb geochronology of potassic felsic intrusions in western Yunnan, SW China: Constraints on the relationship of magmatism to the Jinsha suture: Gondwana Research, v. 22, p. 737–747, https://doi.org/10.1016/j.gr.2011.11.016.

Marcotte, S.B., Klepeis, K.A., Clarke, G.L., Gehrels, G., and Hollis, J.A., 2005, Intra-arc transpression in the lower crust and its relationship to magmatism in a Mesozoic magmatic arc: Tectonophysics, v. 407, p. 135–163, https://doi.org/10.1016/j.tecto.2005.07.007.

Miller, M.S., and Becker, T.W., 2014, Reactivated lithospheric-scale discontinuities localize dynamic uplift of the Moroccan Atlas Mountains: Geology, v. 42, p. 35–38, https://doi.org/10.1130/G34959.1.

Miller, R.B., Paterson, S.R., and Matzel, J.P., 2009, Plutonism at different crustal levels: Insights from the ~5–40 km (paleodepth) North Cascades crustal section, Washington, *in* Miller, R.B., and Snoke, A.W., eds., Crustal Cross Sections from the Western North American Cordillera and Elsewhere: Implications for Tectonic and Petrologic Processes: Geological Society of America Special Paper 456, p. 125–149, https://doi.org/10.1130/2009.2456(05).

Miranda, E.A., and Klepeis, K.A., 2016, The interplay and effects of deformation and crystallized melt on the rheology of the lower continental crust, Fiordland, New Zealand: Journal of Structural Geology, v. 93, p. 91–105, https://doi.org/10.1016/j.jsg.2016.09.007.

Molina-Garza, R.S., Geissman, J.W., Wawrzyniec, T.F., Peña Alonso, T.A., Iriondo, A., Weber, B., and Aranda-Gómez, J., 2015, Geology of the coastal Chiapas (Mexico) Miocene plutons and the Tonalá shear zone: Syntectonic emplacement and rapid exhumation during sinistral transpression: Lithosphere, v. 7, no. 3, p. 257–274, https://doi.org/10.1130/L409.1.

Mortimer, N., 2004, New Zealand's Geological Foundations: Gondwana Research, v. 7, p. 261–272, https://doi.org/10.1016/S1342-937X(05)70324-5.

Mortimer, N., 2008, Zealandia, *in* Spencer, J.E., and Titley, S.R., eds., Ores and Orogenesis: Circum-Pacific Tectonics, Geologic Evolution, and Ore Deposits: Arizona Geological Society Digest 22, p. 227–233.

Mortimer, N., and Campbell, H., 2014, Zealandia: Our Continent Revealed: Rosedale, Auckland, Penguin Random House New Zealand, 272 p.

Mortimer, N., Tulloch, A.J., Spark, R.N., Walker, N.W., Ladley, E., Allibone, A., and Kimbrough, D.L., 1999, Overview of the Median Batholith, New Zealand: A new interpretation of the geology of the Median Tectonic Zone and adjacent rocks: Journal of African Earth Sciences, v. 29, p. 257–268, https://doi.org/10.1016/S0899-5362(99)00095-0.

Mortimer, N., Rattenbury, M.S., King, P.R., Bland, K.J., Barrell, D.J.A., Bache, F., Begg, J.G., Campbell, H.J., Cox, S.C., Crampton, J.S., Edbrooke, S.W, Forsyth, P.J., Johnston, M.R., Jongens, R., Lee, J.M., Leonard, G.S., Raine, J.I., Skinner, D.N.B., Timm, C., Townsend, D.B., Tulloch, A.J., Turnbull, I.M., and Turnbull, R.E., 2014, High-level stratigraphic scheme for New Zealand rocks: New Zealand Journal of Geology and Geophysics, v. 57, no. 4, p. 402–419, https://doi.org/10.1080/00288306.2014.946062.

Mulcahy, S.R., Roeske, S.M., McClelland, W.C., Jourdan, F., Iriondo, A., Renne, P.R., Vervoort, J.D., and Vujovich, G.I., 2011, Structural evolution of a composite middle to lower crustal section: The Sierra de Pie de Palo, northwest Argentina: Structural evolution of the Sierra de Pie de Palo: Tectonics, v. 30, https://doi.org/10.1029/2009TC002656.

Müller, W.F., and Franz, G., 2004, Unusual deformation microstructures in garnet, titanite and clinozoisite from an eclogite of the Lower Schist Cover, Tauern Window, Austria: European Journal of Mineralogy, v. 16, p. 939–944, https://doi.org/10.1127/0935-1221/2004/0016-0939.

Nabavi, S.T., Alavi, S.A., Díaz-Azpiroz, M., Mohammadi, S., Ghassemi, M.R., Fernández, C., Barcos, L., and Frehner, M., 2020, Deformation mechanics in inclined, brittle-ductile transpression zones: Insights from 3D finite element modelling: Journal of Structural Geology, v. 137, 104082, https://doi.org/10.1016/j.jsg.2020.104082.

Naganjaneyulu, K., and Santosh, M., 2011, Geophysical signatures of fluids in a reactivated Precambrian collisional suture in central India: Geoscience Frontiers, v. 2, p. 289–301, https://doi.org/10.1016/j.gsf.2011.06.001.

Needy, S.K., Anderson, J.L., Wooden, J.L., Fleck, R.J., Barth, A.P., Paterson, S.R., Memeti, V., and Pignotta, G.S., 2009, Mesozoic magmatism in an upper- to middle-crustal section through the Cordilleran continental margin arc, eastern Transverse Ranges, California, *in* Miller, R.B., and Snoke, A.W., eds., Crustal Cross Sections from the Western North American Cordillera and Elsewhere: Implications for Tectonic and Petrologic Processes: Geological Society of America Special Paper 456, p. 187–218, https://doi.org/10.1130/2009.2456(07).

Otamendi, J.E., Ducea, M.N., and Bergantz, G.W., 2012, Geological, petrological and geochemical evidence for progressive construction of an arc crustal section, Sierra de Valle Fertil, Famatinian Arc, Argentina: Journal of Petrology, v. 53, p. 761–800, https://doi.org/10.1093/petrology/egr079.

Paterson, S.R., Fowler, T.K., Schmidt, K.L., Yoshinobu, A.S., Yuan, E.S., and Miller, R.B., 1998, Interpreting magmatic fabric patterns in plutons: Lithos, v. 44, p. 53–82, https://doi.org/10.1016/S0024-4937(98)00022-X.

Paterson, S.R., Okaya, D., Memeti, V., Economos, R., and Miller, R.B., 2011, Magma addition and flux calculations of incrementally constructed magma chambers in continental margin arcs: Combined field, geochronologic, and thermal modeling studies: Geosphere, v. 7, p. 1439–1468, https://doi.org/10.1130/GES00696.1.

Philippon, M., and Corti, G., 2016, Obliquity along plate boundaries: Tectonophysics, v. 693, p. 171–182, https://doi.org/10.1016/j.tecto.2016.05.033.

Prowatke, S., and Klemme, S., 2005, Effect of melt composition on the partitioning of trace elements between titanite and silicate melt: Geochimica et Cosmochimica Acta, v. 69, p. 695–709, https://doi.org/10.1016/j.gca.2004.06.037.

Prowatke, S., and Klemme, S., 2006, Rare earth element partitioning between titanite and silicate melts: Henry's law revisited: Geochimica et Cosmochimica Acta, v. 70, no. 19, p. 4997–5012, https://doi.org/10.1016/j.gca.2006.07.016.

Ramezani, J., and Tulloch, A.J., 2009, TIMS U-Pb geochronology of dioritic-granitic rocks Fiordland, http://data.gns.cri.nz/paperdata/index.jsp (accessed 28 October 2014).

Román-Berdiel, T., Gapais, D., and Brun, J.-P., 1997, Granite intrusion along strike-slip zones in experiment and nature: American Journal of Science, v. 297, p. 651–678, https://doi.org/10.2475/ajs.297.6.651.

Rosenberg, C.L., 2004, Shear zones and magma ascent: A model based on a review of the Tertiary magmatism in the Alps: Shear zones and magma ascent: Tectonics, v. 23, no. 3, https://doi.org/10.1029/2003TC001526.

Saint Blanquat, M., Tikoff, B., Teyssier, C., and Vigneresse, J.L., 1998, Transpressional kinematics and magmatic arcs, *in* Holdsworth, R.E., Strachan, R.A., and Dewey, J.F., eds., Continental Transpressional and Transtensional Tectonics: Geological Society of London Special Publication 135, p. 327–340.

Saleeby, J., Ducea, M., and Clemens-Knott, D., 2003, Production and loss of high-density batholithic root, southern Sierra Nevada, California: High-density batholithic root: Tectonics, v. 22, no. 6, https://doi.org/10.1029/2002TC001374.

Sambridge, M.S., and Compston, W., 1994, Mixture modeling of multi-component data sets with application to ion-probe zircon ages: Earth and Planetary Science Letters, v. 128, p. 373–390, https://doi.org/10.1016/0012-821X(94)90157-0.

Sanderson, D.J., and Marchini, W.R.D., 1984, Transpression: Journal of Structural Geology, v. 6, p. 449–458, https://doi.org/10.1016/0191-8141(84)90058-0.

Scott, J.M., and Cooper, A.F., 2006, Early Cretaceous extensional exhumation of the lower crust of a magmatic arc: Evidence from the Mount Irene Shear Zone, Fiordland, New Zealand: Mount Irene Shear Zone, Fiordland: Tectonics, v. 25, no. 3, https://doi.org/10.1029/2005TC001890.

Scott, J.M., and Palin, J.M., 2008, LA-ICP-MS U-Pb zircon ages from Mesozoic plutonic rocks in eastern Fiordland, New Zealand: New Zealand Journal of Geology and Geophysics, v. 51, p. 105–113, https://doi.org/10.1080/00288300809509853.

Scott, J.M., Palin, J.M., and Cooper, A.F., 2009a, A younger age constraint on high-grade metamorphism near George Sound in Fiordland, New Zealand: New Zealand Journal of Geology and Geophysics, v. 52, p. 67–71, https://doi.org/10.1080/00288300909509879.

Scott, J.M., Palin, J.M., Cooper, A.F., Fagereng, Å., and King, R.P., 2009b, Polymetamorphism, zircon growth and retention of early assemblages through the dynamic evolution of a continental arc in Fiordland, New Zealand: Journal of Metamorphic Geology, v. 27, p. 281–294, https://doi.org/10.1111/j.1525-1314.2009.00817.x.

Scott, J.M., Cooper, A.F., Palin, J.M., Tulloch, A.J., Kula, J., Jongens, R., Spell, T.L., and Pearson, N., 2009c, Tracking the influence of continental margin on growth of a magmatic arc in Fiordland, New Zealand using thermobarometry, thermochronology and zircon U-Pb and Hf isotopes: Tectonics, v. 28, no. 6, https://doi.org/10.1029/2009TC002489.

Scott, J.M., Cooper, A.F., Tulloch, A.J., and Spell, T.L., 2011, Crustal thickening of the Early Cretaceous paleo-Pacific Gondwana margin: Gondwana Research, v. 20, p. 380–394, https://doi.org/10.1016/j.gr.2010.10.008.

Schwartz, J.J., Stowell, H.H., Klepeis, K.A., Tulloch, A.J., Kylander-Clark, A.R.C., Hacker, B.R., and Coble, M.A., 2016, Thermochronology of extensional orogenic collapse in the deep crust of Zealandia: Geosphere, v. 12, p. 647–677, https://doi.org/10.1130/GES01232.1.

Schwartz, J.J., Klepeis, K.A., Sadorski, J.F., Stowell, H.H., Tulloch, A.J., and Coble, M.A., 2017, The tempo of continental arc construction in the Mesozoic Median Batholith, Fiordland, New Zealand: Lithosphere, v. 9, p. 343–365, https://doi.org/10.1130/L610.1.

Spencer, K.J., Hacker, B.R., Kylander-Clark, A.R.C., Andersen, T.B., Cottle, J.M., Stearns, M.A., Poletti, J.E., and Seward, G.G.E., 2013, Campaign-style titanite U–Pb dating by laser-ablation ICP: Implications for crustal flow, phase transformations and titanite closure: Chemical Geology, v. 341, p. 84–101, https://doi.org/10.1016/j.chemgeo.2012.11.012.

Stowell, H., Parker, K.O., Gatewood, M., Tulloch, A., and Koenig, A., 2014, Temporal links between pluton emplacement, garnet granulite metamorphism, partial melting and extensional collapse in the lower crust of a Cretaceous magmatic arc, Fiordland, New Zealand: Journal of Metamorphic Geology, v. 32, p. 151–175, https://doi.org/10.1111/jmg.12064.

Sutherland, R., Gurnis, M., and Kamp, P.J.J., 2009, Regional exhumation history of brittle crust during subduction initiation, Fiordland, southwest New Zealand, and implications for thermochronologic sampling and analysis strategies: Geosphere, v. 5, p. 409–425, https://doi.org/10.1130/GES00225.SA2.

Tikoff, B., and Saint Blanquat, M., 1997, Transpressional shearing and strike-slip partitioning in the Late Cretaceous Sierra Nevada magmatic arc, California: Tectonics, v. 16, p. 442–459, https://doi.org/10.1029/97TC00720.

Tikoff, B., and Teyssier, C., 1994, Strain modeling of displacement-field partitioning in transpressional orogens: Journal of Structural Geology, v. 16, p. 1575–1588, https://doi.org/10.1016/0191-8141(94)90034-5.

Tommasi, A., Vauchez, A., Femandes, L.A.D., and Porcher, C.C., 1994, Magma-assisted strain localization in an orogen-parallel transcurrent shear zone of southern Brazil: Tectonics, v. 13, p. 421–437, https://doi.org/10.1029/93TC03319.

Tulloch, A.J., and Kimbrough, D., 2003, Paired plutonic belts in convergent margins and the development of high Sr/Y magmatism: Peninsular Ranges batholith of Baja California and Median Batholith of New Zealand, *in* Johnson, S.E., Paterson, S.R., Fletcher, J.M., Girty, G.H., Kimbrough, D.L., and Martin-Barajas, A., eds., Tectonic Evolution of Northwestern Mexico and the Southwestern USA: Geological Society of America Special Paper 374, p. 275–296, https://doi.org/10.1130/0-8137-2374-4.275.

Tulloch, A.J., Ramezani, J., Kimbrough, D.L., Faure, K., and Allibone, A.H., 2009, U-Pb geochronology of mid-Paleozoic plutonism in western New Zealand: Implications for S-type granite generation and growth of the east Gondwana margin: Geological Society of America Bulletin, v. 121, p. 1236–1261, https://doi.org/10.1130/B26272.1.

Turnbull, I.M., Allibone, A.H., and Jongens, R., 2010, Geology of the Fiordland area: Lower Hutt, New Zealand Institute of Geological and Nuclear Sciences, 97 p., scale 1:250,000.

Turnbull, R., Tulloch, A., Ramezani, J., and Jongens, R., 2016, Extension-facilitated pulsed S-I-A-type "flare-up" magmatism at 370 Ma along the southeast Gondwana margin in New Zealand: Insights from U-Pb geochronology and geochemistry: Geological Society of America Bulletin, v. 128, p. 1500–1520, https://doi.org/10.1130/B31426.1.

Vaughan, A.P.M., Storey, C., Kelley, S.P., Barry, T.L., and Curtis, M.L., 2012, Synkinematic emplacement of Lassiter Coast Intrusive Suite plutons during the Palmer Land Event: Evidence for mid-Cretaceous sinistral transpression at the Beaumont Glacier in eastern Palmer Land: Journal of the Geological Society of London, v. 169, p. 759–771, https://doi.org/10.1144/jgs2011-160.

Whitney, D.L., Teyssier, C., and Vanderhaeghe, O., 2004, Gneiss domes and crustal flow, *in* Whitney, D.L., Teyssier, C., and Siddoway, C.S., Gneiss Domes in Orogeny: Geological Society of America Special Paper 380, p. 15–33, https://doi.org/10.1130/0-8137-2380-9.15.

Zibra, I., Smithies, R.H., Wingate, M.T.D., and Kirkland, C.L., 2014, Incremental pluton emplacement during inclined transpression: Tectonophysics, v. 623, p. 100–122, https://doi.org/10.1016/j.tecto.2014.03.020.